A&A, 681, A23 (2024)
https://doi.org/10.1051/0004-6361/202347670

Astronomy & Astrophysics

Debiased population of very young asteroid families

D. Vokrouhlický[1], D. Nesvorný[2], M. Brož[1], and W. F. Bottke[2]

[1] Institute of Astronomy, Charles University, V Holešovičkách 2, 180 00 Prague 8, Czech Republic
e-mail: vokrouhl@cesnet.cz
[2] Department of Space Studies, Southwest Research Institute, 1050 Walnut St., Suite 300, Boulder, CO 80302, USA

Received 7 August 2023 / Accepted 20 October 2023

ABSTRACT

Context. Asteroid families that are less than one million years old offer a unique possibility to investigate recent asteroid disruption events and test ideas about their dynamical evolution. Observations provided by powerful all-sky surveys have led to an enormous increase in the number of detected asteroids over the past decade. When the known populations are well characterized, they can be used to determine asteroid detection probabilities, including those in young families, as a function of their absolute magnitude.
Aims. We use observations from the Catalina Sky Survey (CSS) to determine the bias-corrected population of small members in four young families down to sizes equivalent to several hundred meters.
Methods. Using the most recent catalog of known asteroids, we identified members from four young families for which the population has grown appreciably over recent times. A large fraction of these bodies have also been detected by CSS. We used synthetic populations of asteroids, with their magnitude distribution controlled by a small number of parameters, as a template for the bias-corrected model of these families. Applying the known detection probability of the CSS observations, we could adjust these model parameters to match the observed (biased) populations in the young families.
Results. In the case of three families, Datura, Adelaide, and Rampo, we find evidence that the magnitude distribution transitions from steep to shallow slopes near 300 to 400 meters. Conversely, the Hobson family population may be represented by a single power-law model. The Lucascavin family has a limited population; no new members have been discovered over the past two decades. We consider a model of parent body rotational fission with the escaping secondary tidally split into two components (thereby providing three members within this family). In support of this idea, we find that no other asteroid with absolute magnitude $H \leq 18.3$ accompanies the known three members in the Lucascavin family. A similar result is found for the archetypal asteroid pair Rheinland–Kurpfalz.

Key words. celestial mechanics – minor planets, asteroids: general

1. Introduction

More than a century ago, Hirayama (1918) discovered the first examples of statistically significant clusters in the space of asteroid heliocentric orbital elements (using proper values of the semimajor axis, eccentricity, and inclination). Suspecting their mutual relation, he coined the term asteroid families. Hirayama rightly proposed that the families are collections of asteroids related to parent bodies that disrupted sometime in the past. He even identified asteroid collisions as the source of these catastrophic events. Over time, asteroid families became a core element of Solar System small body science. They provide (i) an important constraint on asteroid collisional models; (ii) a unique tool to study the internal structure of large asteroids, both in terms of their chemical homogeneity and mechanical structure; (iii) an important source of impactor showers that include both large projectiles and dust onto the surfaces of the terrestrial planets (including the Earth); (iv) an arena for studying a plethora of dynamical processes affecting the orbits and spins of asteroids; and (v) many more (see, e.g., recent reviews by Nesvorný et al. 2015; Masiero et al. 2015; Michel et al. 2015; Novaković et al. 2022).

In this paper, we explore (ii), namely the capability of asteroid family data to constrain the internal structure of the parent body. Over the past two decades or so, sophisticated numerical approaches have been developed to model energetic asteroidal collisions, the subsequent dispersal, and gravitational re-accumulation of resulting fragments (e.g., Michel et al. 2015; Asphaug et al. 2015; Jutzi et al. 2015). The outcome of these simulations, which may be compared to the information provided by asteroid families, sensitively depends on assumptions about the internal properties of the parent body. One type of dataset includes the size frequency distribution of asteroid members in the family. While determining asteroid family members looks straightforward, it has potential complications. This is because many families extend over non-negligible portions of the asteroid belt. As a result, the proper zone in orbital element space in which the family members are located may contain a certain fraction of unrelated (interloping) asteroids. Methods to estimate the interloper fraction have been developed (e.g., Migliorini et al. 1995), but their validity is limited and their results are necessarily of a statistical, rather than deterministic, nature. Additionally, progress from powerful and automated surveys over the past decades makes it more difficult to deal with the interloper problem because small asteroid spatial densities increasely fill proper element space. Unless we know the size distribution of the background and the family population, more asteroids mean that there are more interlopers to deal with.

Fortunately, the ability of surveys to increase the known asteroid populations has also brought into play a new and interesting niche that allows us to determine the complete (bias-corrected) population of the family members. The fundamental goal of this paper is to try to exploit this possibility. Our focus here is on a special subclass of asteroid families characterized

by extremely young ages, namely those that are ≃1 Myr or less. Already the first examples, which were discovered little less than two decades ago (Nesvorný et al. 2006; Nesvorný & Vokrouhlický 2006), help us understand the means to get rid of potential interlopers. Consider that the unusual youth of these families means that five of the six osculating orbital elements are clustered (semimajor axis a, eccentricity e, inclination I, and longitudes of node Ω and perihelion ϖ), rather than the standard three proper orbital elements used for most family work (semimajor axis $a_{\rm p}$, eccentricity $e_{\rm p}$, and inclination $I_{\rm p}$). This immediately has two positive consequences. First, our work can use simpler osculating elements rather than less (population-wise) accessible proper elements. Second, the additional two dimensions of the orbital element arena in which we searched for these very young families have a diluted spatial density of known asteroids. The very young families show up as distinct, and often isolated clusters, allowing us to largely circumvent the interloper problem. Additionally, their recent origin has allowed us to accurately determine each family's age by propagating the asteroid orbits backward in time and then by observing how the orbits rearrange themselves into a tighter cluster at the epoch of its formation. This procedure has helped to further eliminate interlopers.

As far as the population count is concerned, we are then left with the observational bias produced by telescopic limitations (basically the capability of a given instrument to detect asteroids to some apparent magnitude). Here we can compensate for this problem to a degree by using asteroids taken from a well-characterized and sufficiently long-lasting survey. Profiting from our earlier work, in which we developed a new model for the near-Earth asteroid population, we use a careful characterization of the Catalina Sky Survey (1.5-m Mt. Lemmon telescope, G96) observations in between 2016 and 2022. We apply this rich dataset to determine the bias-corrected population of four very young families and a few more clusters of interest[1].

We first briefly describe the observation set in Sect. 2. Next, we introduce the very young families that we are going to analyze in this paper (Sect. 3), providing their new identification and full membership in the Appendix. In Sect. 4, we develop an approach to determine the complete population of the families, based on their biased population and information about the survey detection probability, and we apply it to the selected cases. In Sect. 5, we discuss the implications of our results and provide some discussion of potential future work.

2. Catalina Sky Survey observations

Catalina Sky Survey[2] (CSS), managed by Lunar and Planetary Laboratory of the University of Arizona, has been one of the most prolific survey programs over the past decade (e.g., Christensen et al. 2019). While primarily dedicated to the discovery and further tracking of near-Earth objects with the goal to characterize a significant fraction of the population with sizes as small as 140 m, CSS observations represent an invaluable source of information for other studies in planetary science or astronomy in general.

Here, we use observations of the CSS 1.5-m survey telescope located at Mt. Lemmon (MPC observatory code G96). Our method builds on the work of Nesvorný et al. (2023), who constructed a new model of the near-Earth object population using CSS data. They carried out a detailed analysis of the asteroid detection probabilities for the G96 operations over the period between January 2013 and June 2022. This interval was divided into two phases: (i) observations before May 14, 2016 (phase 1), and (ii) observations after May 31, 2016 (phase 2). The first phase contained 61 585 well-characterized frames, in the form of sequences of four that were typically 30 s exposure images, while the second phase had 162 280 well-characterized frames. The reason for the difference was due to longer timespan of the phase 2 but also an important upgrade of the CSS CCD camera in the second half of May 2016. The new camera had four times the field of view, and better photometric sensitivity, allowing the survey to cover a much larger latitude region about the ecliptic. The superiority of the CSS observations taken during phase 2 allows us to drop the phase 1 data in most of the work below. Only in the case of Lucascavin family and Rheinland-Kurpfalz pair do we combine observations from the two phases into a final result.

The final product of interest for our work here is the detection probability $p(H)$ as a function of the absolute magnitude H for asteroids in a chosen family. In principle, p depends not only on H, but on all orbital elements (in other words, it is specific to a particular body). Members in the youngest known asteroid families to date, however, have their orbit longitudes λ uniformly distributed in between 0° and 360°. This is because the characteristic λ dispersal timescale after the family forming event is only about 1–3 kyr; all families which we consider here are at least an order of magnitude older than this value. Conversely, a property of very young asteroid families are that they have a tight clustering in the other five orbital elements, including the longitude of node Ω and longitude of perihelion ϖ. As a result, the detection probability $p(H)$ assigned to a given family has been computed using the mean values of osculating orbital elements, except for λ where the individual probabilities have been averaged[3]. Only in the case of two families – Datura and Rampo – we used the secular angles Ω and ϖ to randomly sample their observed interval of values shown in Figs. 1 and 9. As seen in those figures, and expected from theoretical considerations, the Ω vs. ϖ values are strongly correlated in very young families. We take this correlation into account when computing the mean detection probability $p(H)$.

Apart from $p(H)$, we can also determine a detection rate $r(H)$, namely a statistically mean number of the survey fields of view in which a given family member with an absolute magnitude H should have been detected. While correlated with $p(H)$, $r(H)$ contains additional information and may be thus used as a consistency check in our analysis below. Technical details of the numerical methods that allow us to determine $p(H)$ and $r(H)$ can be found in Nesvorný et al. (2023).

3. Very young families

In this section we introduce four very young asteroid families, namely Datura, Adelaide, Hobson and Rampo, whose known population is large enough that they are suitable candidates for

[1] The first attempt of the method has been carried out by Vokrouhlický et al. (2017a), who applied it to the case of Datura family. However, both (i) the precise detection efficiency characterization of the older set of Catalina survey observations, and (ii) mainly the Datura family known population, were significantly smaller than in the present paper.

[2] https://catalina.lpl.arizona.edu/

[3] We used 10 000 synthetic orbits characteristic to the family and λ uniformly distributed in its definition interval to determine the mean value of $p(H)$.

Table 1. Asteroid families and pairs studied in this paper.

	Name	N_{obs}	N_{CSS}	Goal
		Very young families 1		
AF	Datura	91	60	Parameters of the bias-corrected population
AF	Adelaide	79	63	Parameters of the bias-corrected population
AF	Hobson	60	33	Parameters of the bias-corrected population
AF	Rampo	42	26	Parameters of the bias-corrected population
		Very young families 2		
AF	Wasserburg	8	8	Possibly steep distribution of small fragments
AF	Martes	6	3	Possibly steep distribution of small fragments
		Special: starving families and pairs		
AF	Lucascavin	3	3	No additional members?
AP	Rheinland/Kurpfalz	2	2	No additional members?

Notes. Very young families 1 with abundant population of known members allow us to estimate parameters of the bias-corrected population. Very young families 2 contain smaller numbers of known members; here we can only indicate steep progression of currently unobservable members. Starving families and asteroid pairs contain up to three members only; here we aim at disproving additional members with absolute magnitude smaller than some threshold. The first column identifies the asteroid category: AF for the asteroid family, AP for the asteroid pair. The second column provides the name, the third and fourth column give number of known members and number of members detected by Catalina Sky Survey. The last column states in brief our goals in this work.

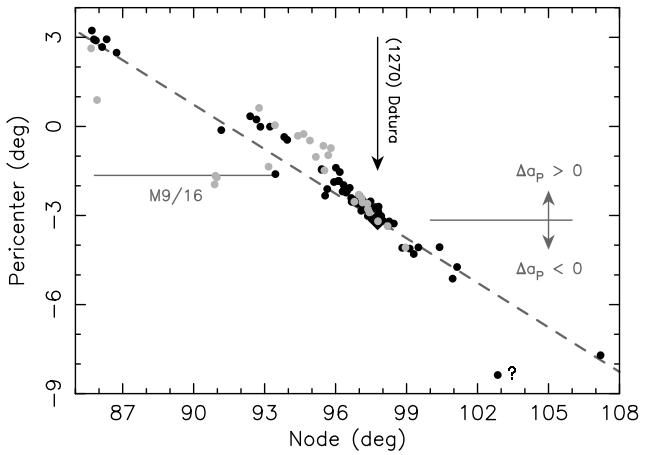

Fig. 1. Osculating values of the secular angles – longitude of node Ω (abscissa) and longitude of perihelion ϖ (ordinate) – for members in the Datura family (epoch MJD 60 000.0). The black symbols show multi-opposition orbits, gray symbols are for the singleopposition orbits; diamond symbol for (1270) Datura, the largest member. Larger/smaller relative values of the secular angles, measured with respect to (1270) Datura, are correlated with positive/negative shift in proper semimajor axis Δa_P (as explained by the arrows). Because the node drifts in a retrograde sense, while the perihelion drifts in the prograde sense, their trends are opposite to each other (thence anticorrelation of the two angles). Location of the exterior mean motion resonance M9/16 with Mars is mapped where the label shows. The dashed line with a slope −0.5 indicates the (anti-) correlation trend. The symbol indicated by a question mark shows projection of (429988) 2013 PZ36 (an object captured on a very chaotic orbit possibly in the exterior mean motion resonance E3/10 with Earth), whose association to the Datura family is uncertain.

our debiasing efforts[4]. We also consider two additional families, Wasserburg and Martes, that have extremely young ages but whose population is limited. For these examples, we do not perform a full-scale debiasing analysis but instead argue that a large population of small undetected members should exist near the currently known population. Finally, we consider two special cases: the very young asteroid family Lucascavin and the asteroid pair Rheinland–Kurpfalz. Here, our goal is actually opposite to the previous cases. Our working hypothesis is that further smaller fragments in their location might not exist. As a result, we use CSS observations to set an upper limit on the size or magnitude of the unseen members to explore whether this hypothesis might be correct.

Table 1 provides a basic overview of the asteroid clusters and pairs that are analyzed in this paper, as well as some notes on the goals we hope to achieve. The identification method used to find the families, and full listing of the family members for each family analyzed in this paper, is provided in the Appendix. In what follows, we provide basic information about the investigated families, with slightly more attention paid to the Datura family. The debiasing procedure to constrain a complete population of members in the above-mentioned families is presented in the next Sect. 4.

3.1. Very young families with large population of members

Datura. The cluster of asteroids about the largest member (1270) Datura is an archetype of very young families. In this sense it is comparable to the Karin family, which is an excellent example of a sizable young family having an age less than ≃10 Myr but secular angles distributed uniformly in the 0° to 360° interval. Not only is the Datura family the first example discovered in the very young family class (Nesvorný et al. 2006, see also Nesvorný & Vokrouhlický 2006), but its location in the inner part of the main belt allowed us to readily collect the physical parameters of the largest members and study the role of the very young families in a broader context of planetary science (e.g., Mothé-Diniz & Nesvorný 2008; Vernazza et al. 2009; Vokrouhlický et al. 2008, 2009, 2017a). The number of known members in the Datura family has also grown quickly from only 7 in 2006 to 17 in 2017.

Here we make use of the accelerating pace with which asteroids have been discovered during recent years and report a

[4] Obviously, a second criterion of their selection is that CSS detected a significant fraction of known members in these families during its phase 2 operations.

currently known Datura population of $N_{obs} = 91$ members (possibly even 94 members, see Table A.1). Importantly, $N_{CSS} = 60$ of them has been also detected by CSS during its phase 2 operations. We note that Vokrouhlický et al. (2017a) already attempted to use CSS observations for their Datura population debiasing efforts. Our current work, however, surpasses the detail and accuracy of this earlier work. Vokrouhlický et al. (2017a) could use only the 13 largest members in the Datura family detected by CSS between 2005 and 2012. Thanks to the camera update by CSS in 2016, the six years of CSS operations between 2016 and 2022 has led to a much larger Datura population and an improved characterization of family member detection probabilities.

Before we turn our attention to the magnitude distribution of the Datura members, we use this family to exemplify some common features of very young clusters. They help to justify membership of given asteroids within the family, even without a further substantiation via a detailed study of their past orbital convergence using numerical integrations (see a brief discussion of this issue in the Appendix). A correlation between the osculating values of the secular angles, namely longitude of node Ω and longitude of perihelion ϖ, is a characteristic property of several very young families (unless the family is extremely young, such that Ω and ϖ are clustered within a degree or so, basically corresponding to their initial dispersal). Denoting $\Delta\Omega$ and $\Delta\varpi$ as the angular difference with respect to the largest body in the family, the initial phase of the dispersal process is described by a linear approximation. Thus at time T, one has $\Delta\Omega(T) \simeq C\,T + O(T^2)$ and a similar equation for the longitude of perihelion, with $C = (\partial s/\partial a)\,\Delta a$, where s is the proper nodal frequency and Δa is the difference in semimajor axis with respect to the largest body produced by the initial velocity ejection. The smallest observed fragments in Datura have $\Delta a \simeq 2 \times 10^{-3}$ au, corresponding to their ejection by $\simeq$10 m s^{-1} (only slightly larger than the escape velocity from the parent body of the family). Together with $(\partial s/\partial a) \simeq 40$ arcsec yr^{-1} au^{-1}, we can estimate their angular difference $\Delta\Omega \simeq 11^\circ$ in $T \simeq 500$ kyr (see Fig. 1). A similar analysis for $\Delta\varpi$ results in about half this value.

Given that in both $\Delta\Omega$ and $\Delta\varpi$ the nonlinear terms in time T are still very small (those will be produced by the Yarkovsky drift in semimajor axis of the small members in the family; e.g., Vokrouhlický et al. 2009, 2017a), they are strongly correlated with a slope −0.5. The early dispersal phase of very young families is characterized by additional correlations between the osculating elements, namely (i) the eccentricity and longitude of perihelion, and (ii) the inclination and the longitude of node (see, e.g., data in the tables given in the Appendix). As mentioned above, these extra correlations between osculating orbital elements help to strengthen justification of the membership in the family.

The cumulative magnitude distribution $N(< H)$ of Datura family members is shown in Fig. 2. The magnitudes H for the six lowest-numbered members were determined accurately using calibrated observations, and expressed at the mid-value of the lightcurve, by Vokrouhlický et al. (2009, 2017a). The magnitudes for other Datura members were taken from the MPC catalog. We show both the distribution of all known members (black symbols), and highlight also the sample of 60 members which have been detected by CSS (red symbols). Data for these asteroids may be used for debiasing of the Datura family population, since only for them we have the detection probability well characterized.

The bottom panel of Fig. 2 shows detection probability $p(H)$ of Datura members as a function of their absolute magnitude. As explained above, this is a result based on an analysis of 10 000

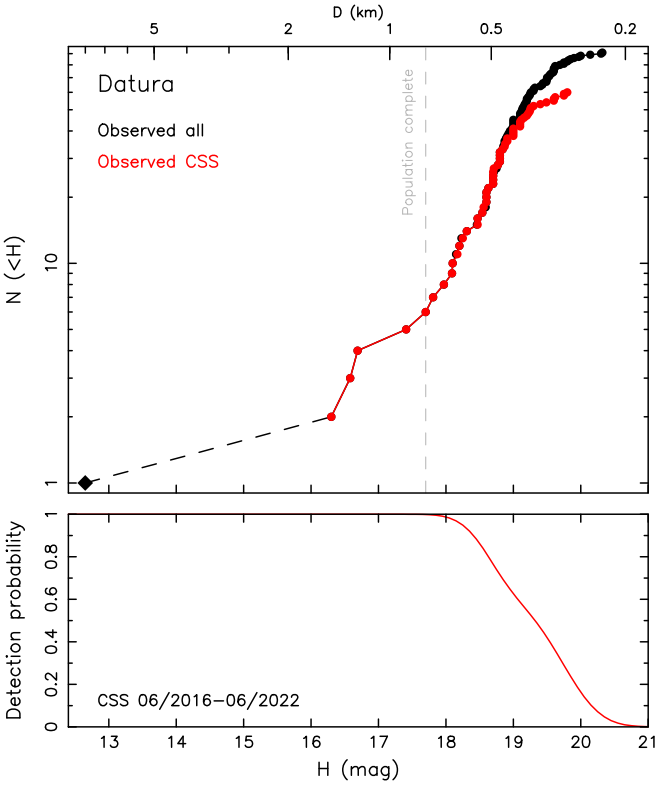

Fig. 2. Top panel: cumulative magnitude distribution $N(< H)$ of the Datura family members. The black symbols are all 91 known members (including the largest asteroid (1270) Datura shown by the diamond, but disregarding (429988) 2013 PZ36, whose membership in the family is uncertain); the red symbols are 60 members detected by CSS during the phase 2 operations. The top abscissa indicates an approximate size computed from H with an assumption of $p_V = 0.24$ value of the geometric albedo. Bottom panel: detection probability $p(H)$ of Datura members as a function of H during the phase 2 operations of CSS based on analysis of geometric and photometric detection factors ran on a large synthetic population of Datura members. We find that $p = 1$ up to $H \simeq 18$ magnitude, which sets the limit where the Datura population is complete (dashed line on the upper panel). Beyond this limit p decreases to zero at about 21 magnitude.

synthetic orbits in the Datura family zone which makes $p(H)$ very smooth. At the first sight, it might be surprising that $p \simeq 1$ up to magnitude 18, signaling that the population of the family members is complete up to that limit. This inference, however, is correct and a result of (i) a six year survey , (ii) the small value of Datura-like orbital inclinations, such that CSS fields-of-view did not miss an opportunity to detect the asteroids in the Datura family, and (iii) a typical 50% photometric detection limit of CSS in between 20.5 and 21.5 apparent magnitude (in the visual bands). Neglecting a small phase-angle correction in the Pogson's relation between absolute H and apparent m magnitudes, we have $H \simeq m - 5\log(r\,\Delta)$, where r and Δ are heliocentric and geocentric distances of the asteroid. At opposition, and near aphelion to cover the worst case situation, we have $r \simeq 2.7$ au and $\Delta \simeq 1.7$ au. As a result, the limiting magnitude $m \simeq 21$ translates to $H \simeq 17.8$. During the 6 yr period of CSS phase 2, the configuration eventually becomes favorable to detection, explaining the completion limit at $H \simeq 18$ magnitude. At the opposite end of things, the probability p has a tail to nearly 21 magnitude. This means CSS with its best nightly limits near the apparent 22 magnitude have a chance to detect small

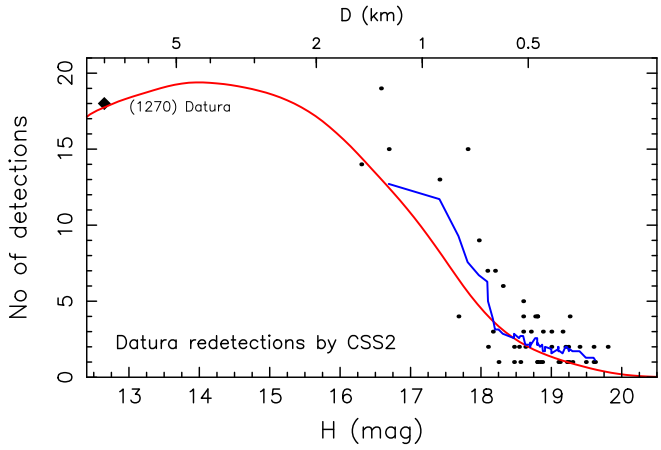

Fig. 3. Number of detections of the identified Datura family members during the phase 2 CSS operations: the largest body (1270) Datura shown by a diamond symbol and highlighted using a label, other 59 smaller members shown by black symbols. The red line is the theoretical prediction based on a large synthetic Datura population computed together with the detection probability $p(H)$ from Fig. 2. The blue curve is a mean number of detections for the observed Datura members computed on a running window of 7 consecutive data-points.

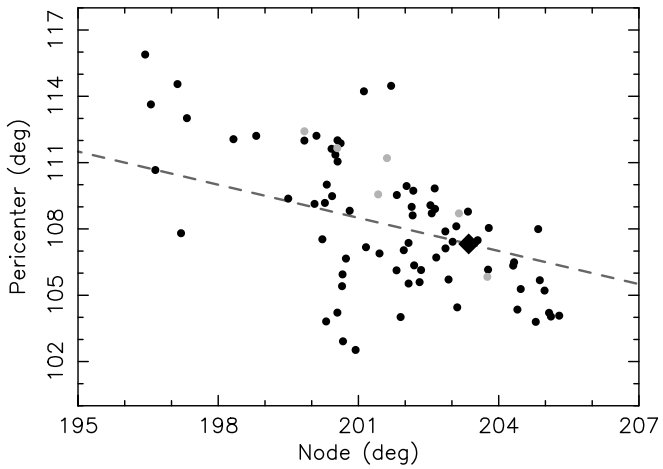

Fig. 4. Osculating values of the secular angles – longitude of node Ω (abscissa) and longitude of perihelion ϖ (ordinate) – for members in the Adelaide family (epoch MJD 60 000.0). The black symbols show multiopposition orbits, gray symbols are for the singleopposition orbits; diamond symbol for (525) Adelaide, the largest member. The dashed line has the expected slope −0.5 (see, e.g., Figs. 1 and 9 for Datura and Rampo families), but the data are more scattered in the Adelaide case. This is likely due to Mars perturbation discussed in Vokrouhlický et al. (2021b).

Datura members when they happen to be near the perihelion of their orbit at opposition.

In order to verify that the detection probability $p(H)$ shown in Fig. 2 is reasonable, we also determined the expected mean rate $r(H)$ of CSS phase 2 detections and compared it with the actual number of detections of all 60 identified Datura members. This result is presented in Fig. 3. The largest body (1270) Datura was found to be detected 18 times, and even members up to magnitude $H = 18$ were typically detected more than 10 times. This is a good verification of population completeness. Only after that limit does the number of detections decrease, with no Datura member having $H > 20$ magnitude detected. This outcome corresponds to the inferred detection probability: $p < 0.1$ for $H > 20$.

The mean value of the actual Datura-member detections computed using a running window of consecutive 7 asteroids is shown by the blue curve. The scatter of the number of detections about the predicted red line is not surprising because the latter has been computed as a mean value from 10 000 synthetic Datura members. The important point is that the blue curve, though computed as a mean over a much smaller number of cases (additionally having different H values), reasonably follows the predicted mean rate. This points to consistency in evaluation of the detection probability too.

Adelaide. The cluster of five small objects about the inner main belt asteroid (525) Adelaide was first reported by Novaković & Radović (2019). Apart from an approximate age of 500 kyr, few details were given in this paper. Carruba et al. (2020), while trying to search for secondary subclusters in the very young asteroid families, analyzed the Adelaide family and identified 19 of its members. The case was finally revisited by Vokrouhlický et al. (2021b), who noted a significant population increase to about 50 small asteroids in this family. They confirmed the earlier age estimate and considered a possibility of a causal link between formation of the Datura and Adelaide families (which they rejected). Novaković et al. (2022) identified already 72 members, and our current census of the Adelaide family population reveals $N_{\rm obs} = 79$ members, yet another important increase. The population increase rate of the Adelaide family is among the largest of the very young families. A fortunate circumstance for our analysis is that $N_{\rm CSS} = 63$ of the members were also detected by CSS in its phase 2.

Figure 4 shows the osculating secular angles Ω and ϖ of the Adelaide family population from Table A.2. The Ω vs. ϖ correlation is weaker than that of the Datura-family members (Fig. 1). Vokrouhlický et al. (2021b), while analyzing behavior of the backward propagated orbits in the Adelaide family, noted a weak chaotic signature triggered by a conjoint effect of weak mean-motion resonances and distant encounters with Mars. We suspect they are also the origin of the observed scatter in the correlation between the secular angles seen in Fig. 4. Nevertheless, the orbits show a high degree of clustering even in the subspace of the secular angles, which in effect strengthens their membership in the family.

The cumulative magnitude distribution of the Adelaide members is shown in Fig. 5. Its extreme behavior has been already noted by Vokrouhlický et al. (2021b): (i) the largest remnant (525) Adelaide is separated from other members in the family by an unusually large gap of 6 magnitudes in the absolute magnitude H scale, and (ii) the small fragment population has an extremely steep H-distribution in between 18 and 19 (the local power-law $N(< H) \propto 10^{\gamma H}$ approximation requires $\gamma \simeq 2$ or even larger). This shape is characteristic of a cratering event on (525) Adelaide.

The bottom panel in Fig. 5 shows the mean detection probability $p(H)$ of the Adelaide members. The range in which $p(H)$ drops from one to zero, namely $H \simeq 18.4$ to $H \simeq 20.4$ magnitudes, is narrower than in the case of the Datura family (with the completion limit at even higher magnitude). This is readily explained by a smaller eccentricity of Adelaide-like orbits for nearly the same value of semimajor axis and inclination.

To further check our results, we also compared the number of CSS phase 2 detections of the 63 Adelaide members and their mean computed rate $r(H)$ (Fig. 6). The largest asteroid (525) Adelaide has been detected 8 times, which conforms – within

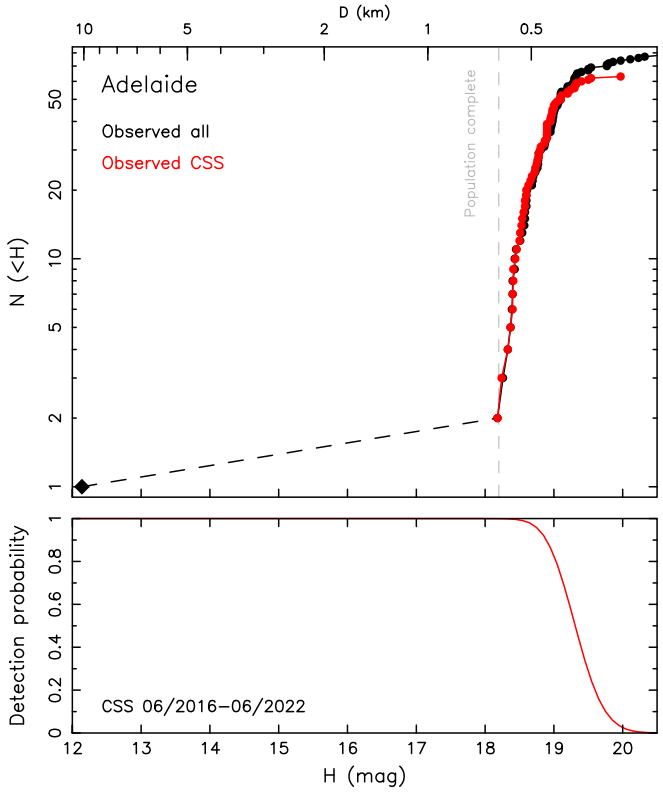

Fig. 5. Top panel: cumulative magnitude distribution $N(< H)$ of the Adelaide family members. The black symbols are all 79 known members (including the largest asteroid (535) Adelaide shown by the diamond), the red symbols are 63 members detected by CSS during the phase 2 operations. The top abscissa indicates an approximate size computed from H with an assumption of $p_V = 0.24$ value of the geometric albedo. Bottom panel: detection probability $p(H)$ of Adelaide members as a function of H during the phase 2 operations of CSS based on analysis of geometric and photometric detection factors ran on a large synthetic population of Adelaide members. We find that $p = 1$ up to $H \simeq 18.2$ magnitude, which sets the limit where the Adelaide population is complete (dashed line on the upper panel). Beyond this limit p decreases to zero at about 20.4 magnitude.

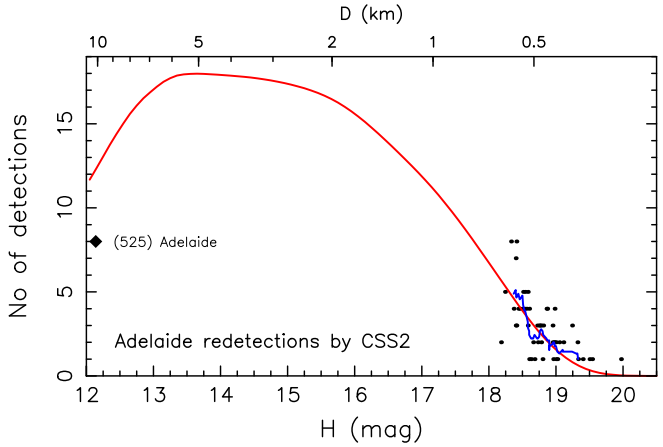

Fig. 6. Number of detections of the identified Adelaide family members during the phase 2 CSS operations: the largest body (525) Adelaide shown by a diamond symbol and highlighted using a label, other 62 smaller members shown by black symbols. The red line is the theoretical prediction based on a large synthetic Adelaide population computed together with the detection probability $p(H)$ from Fig. 5. The blue curve is a mean number of detections for the observed Adelaide members computed on a running window of 9 consecutive data-points.

fluctuation – to the predicted rate of about 13. We note the decrease of $r(H)$ for objects brighter than magnitude 13. This phenomenon in the CSS observations has to do with the saturation of the signal for bright objects, as they can become confused with stationary sources hiding their sky-plane motion. Such a configuration may occasionally happen when (525) Adelaide is at opposition near perihelion of its orbit. Small members then sample the tail of $r(H)$ values with only few detections predicted. The running mean of detections (blue curve) appears to follow the predicted $r(H)$ dependence reasonably well.

Hobson. Pravec & Vokrouhlický (2009) identified a small cluster of asteroids associated with the largest member (57738) 2001 UZ160 and set an upper age of 500 kyr for its formation event. They also noted a nearby asteroid (18777) Hobson, but were unsure about its relation to the cluster, mainly because Hobson and 2001 UZ160 have similar sizes, which they considered unusual for the outcome of a collisional fragmentation of the parent body. Rosaev & Plávalová (2016, 2017, 2018) then revisited the situation and proved that Hobson was associated with the cluster. They derived an age for the family of 365 ± 67 kyr. By 2018, their Hobson population consisted of nine members, which shortly improved to 11 by the work of Pravec et al. (2018). These latter authors also rejected the possibility of the Hobson family formation by rotation fission, and conducted valuable photometric observations of the two largest members Hobson and 2001 UZ160. The two similar-size largest remnants also intrigued Vokrouhlický et al. (2021a), who revisited the nature of the parent object of this family (counting already 45 Hobson members, and Novaković et al. (2022) reported another increase to 51 members). Using the SPH/N-body formation simulation, their results implied a very special impact and target combination was required. As a novel idea, they also argued the Hobson family may result from collisional fragmentation of a component in a parent binary. In this work we report $N_{obs} = 60$ members (likely even one more, see Table A.3), out of which $N_{CSS} = 33$ were detected during the phase 2 of CSS operations.

The dispersion of the secular angles within about two degrees is a consequence of the very young age of the Hobson family. We thus turn our attention directly to the cumulative magnitude distribution of its members shown on Fig. 7. The two largest asteroids – (18777) Hobson and (57738) 2001 UZ160 – are its most outstanding feature. Their orbital convergence has been independently verified by Rosaev & Plávalová (2017, 2018) and Vokrouhlický et al. (2021a), while Pravec et al. (2018) determined the identical values of the $V - R$ color index (compliant with the S-type taxonomy). As a result, their membership to the cluster appears to be solid.

The bottom panel on Fig. 7 shows the mean detection probability $p(H)$ determined for the CSS phase 2 operations. It appears similar to that of the Datura family except for about a magnitude shift towards smaller H, which implies completion down to $H \simeq 17.1$ magnitude. This result is easily understood by a comparison with the Datura family; Hobson's family has similar eccentricity and inclination values, but a larger set of semimajor axis values. The Hobson family resides in the central part of the main asteroid belt next to the J3/1 mean motion with Jupiter.

The inferred mean rate of detections $r(H)$ for the phase 2 of CSS matches, within the statistical fluctuations, the actual number of detections of Hobson members (Fig. 8). The brightest two

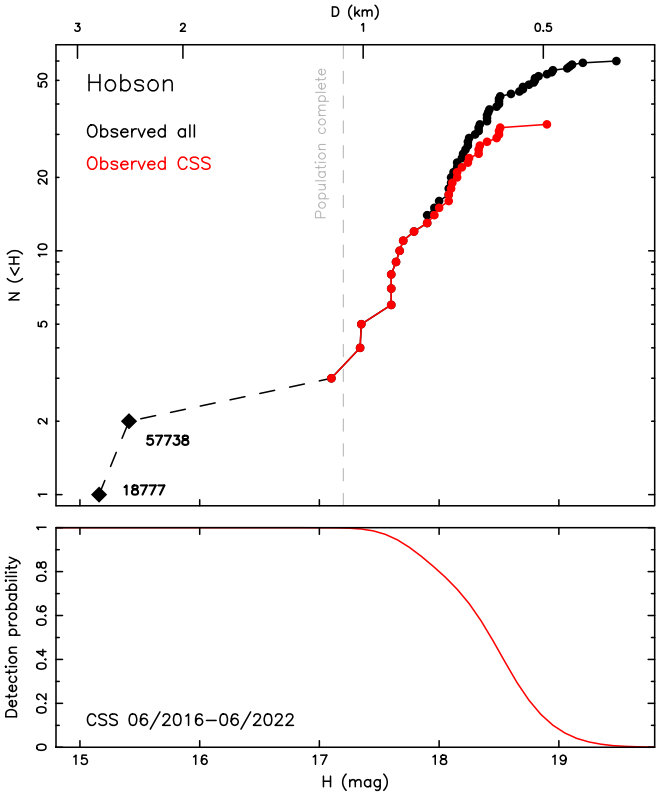

Fig. 7. Top panel: cumulative magnitude distribution $N(< H)$ of the Hobson family members. The black symbols are all 60 known members (including the largest asteroids (18777) Hobson and (57738) 2001 UZ160 shown by the diamond), the red symbols are 33 members detected by CSS during the phase 2 operations. The top abscissa indicates an approximate size computed from H with an assumption of $p_V = 0.2$ value of the geometric albedo. Bottom panel: detection probability $p(H)$ of Hobson members as a function of H during the phase 2 operations of CSS based on analysis of geometric and photometric detection factors ran on a large synthetic population of Hobson members. We find that $p = 1$ up to $H \simeq 17.2$ magnitude, which sets the limit where the Hobson population is complete (dashed line on the upper panel). Beyond this limit p decreases to zero at about 19.5 magnitude.

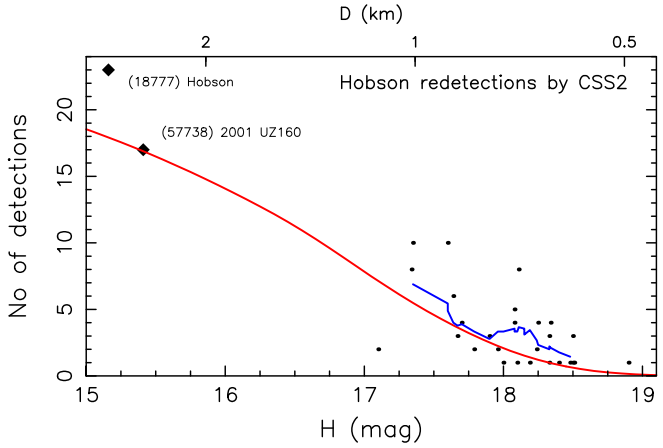

Fig. 8. Number of detections of the identified Hobson family members during the phase 2 CSS operations: the largest bodies (18777) Hobson and (57738) 2001 UZ160 shown by a diamond symbol and highlighted using a label, other 31 smaller members shown by black symbols. The red line is the theoretical prediction based on a large synthetic Hobson population computed together with the detection probability $p(H)$ from Fig. 7. The blue curve is a mean number of detections for the observed Hobson members computed on a running window of 9 consecutive datapoints.

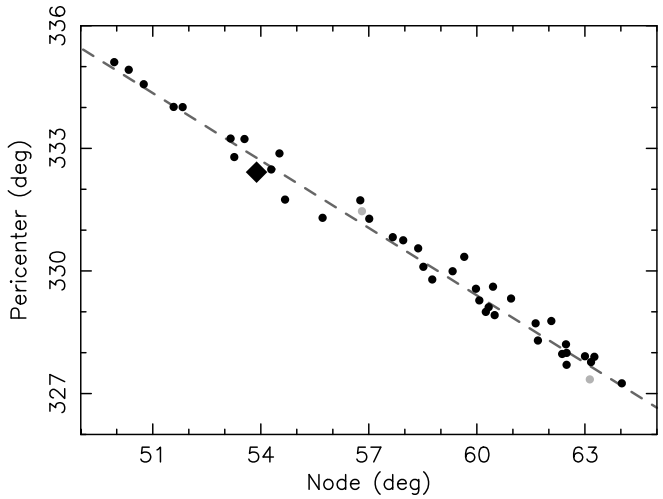

Fig. 9. Osculating values of the secular angles – longitude of node Ω (abscissa) and longitude of perihelion ϖ (ordinate) – for members in the Rampo family (epoch MJD 60 000.0). The black symbols show multiopposition orbits, gray symbols are for the singleopposition orbits; diamond symbol for (10321) Rampo, the largest member. Larger/smaller relative values of the secular angles, measured with respect to (10321) Rampo, correlated with positive/negative shift in proper semimajor axis. The node/perihelion trends are opposite, because the node drift in a retrograde sense, while the perihelion drifts in the prograde sense. The dashed line with a slope −0.5 indicates the correlation trend.

asteroids stand out with more than 15 detections, while members in the small-size tail typically have fewer than five detections.

Rampo. The core of this family, namely two small asteroids tightly clustered about (10321) Rampo, has been found by Pravec & Vokrouhlický (2009). Focusing on asteroid pairs, these authors reported a probable age between 0.5 and 1.1 Myr. About a decade later, Pravec et al. (2018) discovered another four small members in this family and used backward orbital integration to assess a more accurate age of 780^{+130}_{-90} kyr. Finally, Novaković et al. (2022) revisited the Rampo family population and identified 36 small members around the largest remnant (10321) Rampo. Here we find the Rampo family population has increased to $N_{obs} = 42$ (possibly even 44, see Table A.4); $N_{CSS} = 26$ of them were detected during CSS phase 2.

The correlation of the secular angles Ω and ϖ, shown in Fig. 9, is exemplary among the very young families. The family must be still in the dispersion regime that is linear with time (i.e., the same discussed for the Datura family). Similarly to the Datura case, the orbits of Rampo family members exhibit strong correlations in the pairs of orbital elements e vs. ϖ and I vs. Ω, providing us with a useful justification for their family membership.

The cumulative magnitude distribution of Rampo family members shares some similarities with the Datura cluster; compare Figs. 10 and 2. The small differences consist of: (i) a larger magnitude gap ΔH between the largest members and the second largest member ($\Delta H \simeq 3.8$ for Datura and $\Delta H \simeq 3.2$ for Rampo), and (ii) a larger size of (1270) Datura over (10321) Rampo (by about a factor ≃2.15 accounting for a slight albedo difference

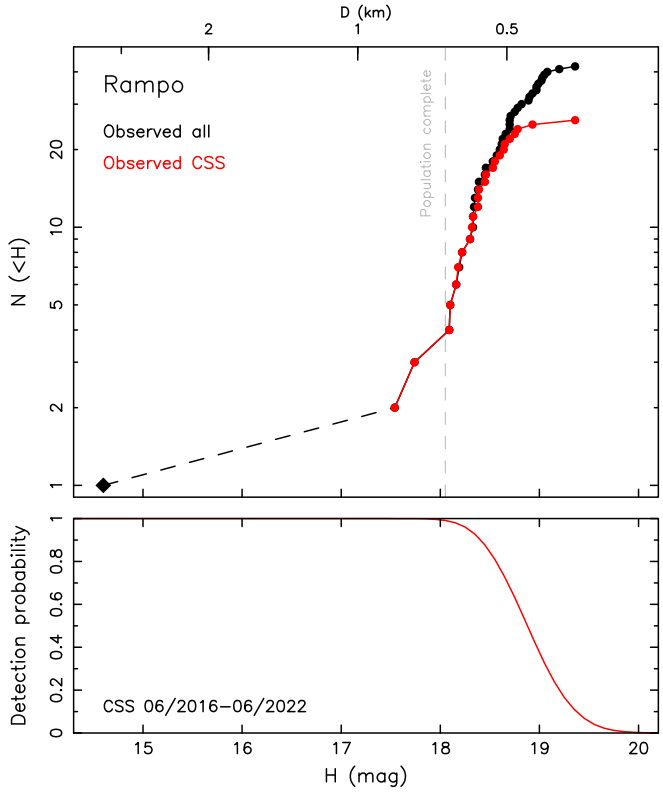

Fig. 10. Top panel: cumulative magnitude distribution $N(< H)$ of the Rampo family members. The black symbols are all 42 known members (including the largest asteroid (10321) Rampo shown by the diamond), the red symbols are 26 members detected by CSS during the phase 2 operations. The top abscissa indicates an approximate size computed from H with an assumption of $p_V = 0.24$ value of the geometric albedo. Bottom panel: detection probability $p(H)$ of Rampo members as a function of H during the phase 2 operations of CSS based on analysis of geometric and photometric detection factors ran on a large synthetic population of Rampo members. We find that $p = 1$ up to $H \simeq 18$ magnitude, which sets the limit where the Rampo population is complete (dashed line on the upper panel). Beyond this limit p decreases to zero at about 20 magnitude.

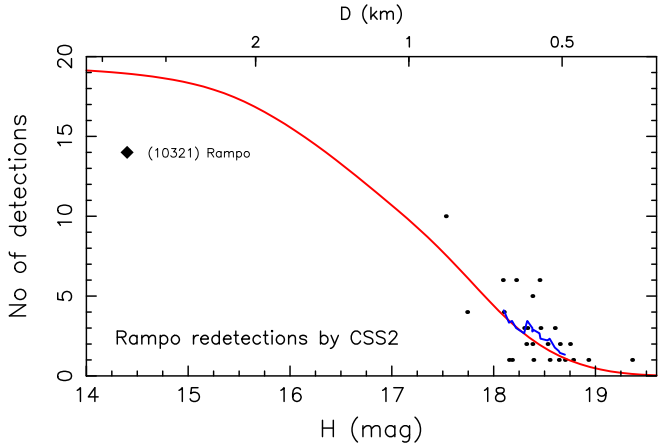

Fig. 11. Number of detections of the identified Rampo family members during the phase 2 CSS operations: the largest body (10321) Rampo shown by a diamond symbol and highlighted using a label, other 25 smaller members shown by black symbols. The red line is the theoretical prediction based on a large synthetic Rampo population computed together with the detection probability $p(H)$ from Fig. 10. The blue curve is a mean number of detections for the observed Rampo members computed on a running window of 9 consecutive data-points.

Pravec et al. 2018, both being S-class spectral taxonomy). Similar to Datura, the former feature suggests that the family may have been formed by a large cratering event, though more work on this issue is required (e.g., Durda et al. 2007). The Rampo members have a detection probability $p(H)$ computed for phase 2 of CSS transitions that go from one at $H \simeq 18$ to zero at $H \simeq 20$. This sharp transition is due to their small eccentricities. The completion limit is similar for both families because their aphelion distances are comparable (on the other hand, the perihelion distance is smaller for Datura orbits and thus its $p(H)$ reaches to larger absolute magnitudes). As in all cases discussed in this paper, the number of CSS phase 2 detections of Rampo family members nicely follows the predicted rate $r(H)$ (Fig. 11).

3.2. Extremely young asteroid families with small numbers of known members

Wasserburg. A very tight asteroid pair of two Hungaria objects (4765) Wasserburg and 2001 XO105 was reported by Vokrouhlický & Nesvorný (2008). Pravec et al. (2010), analyzing the formation process of asteroid pairs, included this couple in their sample and reported an approximate age larger than 90 kyr. Pravec et al. (2019), compiling the most detailed study of the asteroid pair population, noted a small asteroid 2016 GL253 accompanying the pair on a very close orbit and suggested the trio of asteroids may be the large-end tip of a very young family in the Hungaria population. Novaković et al. (2022) confirmed the trend, detecting six members in what they called the Wasserburg family. Here we find two more members in the family, completing the count at $N_{obs} = 8$. Interestingly, all of them were also detected during phase 2 of the CSS operations, thence $N_{CSS} = 8$.

The cumulative magnitude distribution of the presently known members of the Wasserburg family is shown in Fig. 12. The bottom panel on the same figure provides the detection probability $p(H)$ during CSS phase 2 operations. The completion limit is near $H \simeq 18.5$ magnitude, impressively large in spite of the high inclination of the Wasserburg family orbits (being part of the Hungaria zone). Some of these orbits may be missed by the fields-of-view of CSS. The situation improved after July 2016, however, with the wide field camera reaching well beyond the ±30° zone around the ecliptic. So the geometric losses are small, and the heliocentric proximity of the Hungaria region helped to detect even small asteroids. Indeed, the six smallest members in the Wasserburg family have an absolute magnitude near or even above the $H = 19$ limit.

As mentioned in the preamble of this section, the small number of identified members in this family does not permit a full-scale debiasing effort. Accordingly, we only conducted the simplest estimate to characterize the complete Wasserburg population using the following steps:

- We considered the observed (biased) population of the family members and sorted their absolute magnitude values $\{H_i\}$, with $i = 1, \ldots, N_{obs}$, from the smallest to the largest value;
- By definition, the observed population increases by one when shifting along the list according to the ordered H-values; we assume the largest member in the family is bright enough such that $p(H_1) = 1$;
- The simplest estimate of the complete population is then obtained by again moving along the vector $\{H_i\}$ of ordered

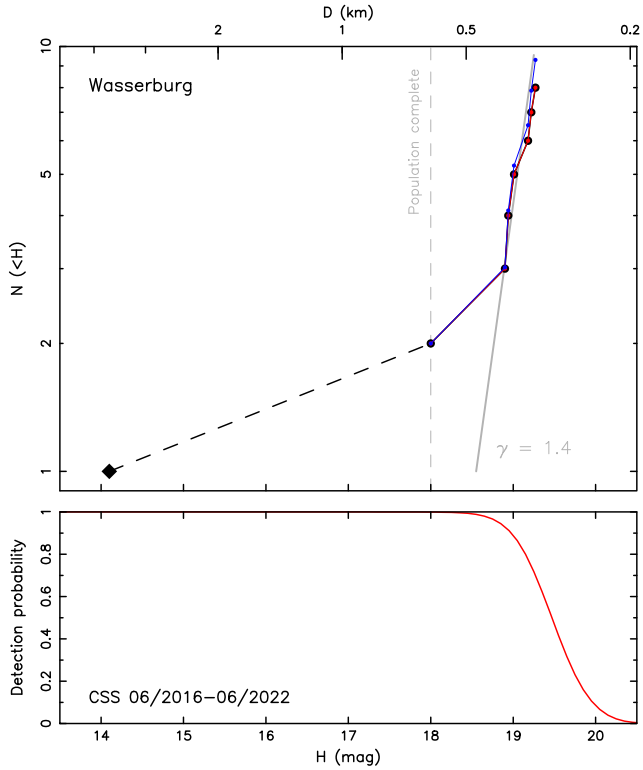

Fig. 12. Top panel: cumulative magnitude distribution $N(< H)$ of the Wasserburg family members. The black symbols are all 8 known members (including the largest asteroid (4765) Wasserburg shown by the diamond), the blue symbols provide the simplest variant of the debiased population. This was obtained by incrementing the population by $1/p(H_{i+1})$, when stepping from absolute magnitude H_i to H_{i+1} ($i = 1, \ldots, N_{\rm obs}$); the observed (biased) population increments by one by definition. The gray line is an approximate local power-law representation $N(< H) \propto 10^{\gamma H}$ near $H \simeq 19$ with $\gamma \simeq 1.4$. The top abscissa indicates an approximate size computed from H with an assumption of $p_{\rm V} = 0.3$ value of the geometric albedo. Bottom panel: Detection probability $p(H)$ of Wasserburg members as a function of H during the phase 2 operations of CSS based on analysis of geometric and photometric detection factors run on a large synthetic population of Wasserburg members. We find that $p = 1$ up to $H \simeq 18.3$ magnitude, which sets the limit where the Wasserburg population is complete (dashed line on the upper panel). Beyond this limit p decreases to zero at about 20.5 magnitude.

absolute magnitudes, but now incrementing the population by $1/p(H_i)$ instead of one.

The result is shown by the blue curve at the top panel of Fig. 12. Since even the smallest Wasserburg fragment has $p(H_8) \simeq 0.71$ (in other words, detection of even the smallest known fragments is expected), the complete population does not deviate too much from the observed population. Up to that point the cumulative magnitude distribution is very steep, locally approximated by a power law with an exponent of $\gamma \simeq 1.4$. This value is only slightly shallower than that observed in the case of the Adelaide family. From that similarity, we may tentatively conclude that Wasserburg family has resulted from a huge cratering event in (4765) Wasserburg itself, though again there are many additional possibilities (e.g., Durda et al. 2007).

However, an outstanding puzzle here is to explain why the current surveys have yet to detect any smaller fragments. This reason is because of the inferred steepness of the magnitude distribution, and the non-negligible detection probability $p(H_8)$ mentioned above. In other words, a fair number of the subsequent members in the Wasserburg family should have a detection probability ≃0.5, yet none have been detected. Does this mean that the magnitude distribution beyond the detected population suddenly becomes shallow. The answer to this question is left for future analysis.

Martes. Vokrouhlický & Nesvorný (2008) mentioned (5026) Martes and 2005 WW113 among their list of tight asteroid pairs. As also noted by these authors, some of these pairs were expected to be the two largest members in a collisionally born asteroid family (e.g., Wasserburg family). Recently, Novaković et al. (2022) reported a third member in the tight orbital region about Martes, namely 2010 TB155, while our census in this paper increases the number by three more small objects, with $N_{\rm obs} = 6$ (Table A.6), with the last three asteroids associated with the Martes cluster discovered in Autumn 2022[5]. Only the largest three members in the Martes family were detected by CSS, such that $N_{\rm CSS} = 3$. The Martes cluster is a part of a much larger Erigone family, whose age has been estimated to ≃280 Myr (e.g., Vokrouhlický et al. 2006; Spoto et al. 2015) or 130 ± 30 Myr by Bottke et al. (2015b). This association is justified by the objects having the same spectral taxonomic type Ch as the Erigone family and (5026) Martes (Polishook et al. 2014). The extremely clustered orbital elements of the Martes members suggest an unusually young age for the family. Indeed, Pravec et al. (2019) found 18 ± 1 kyr, a slight improvement on the result of Pravec et al. (2010). We find that the orbits of the smallest three members may also converge to this time window, further justifying the Martes age, but a detailed analysis would need to consider the thermal accelerations in the simulation. We leave this effort to a separate study, but conclude here that the Martes family has the youngest currently known age.

Figure 13 shows the absolute magnitude distribution of the Martes family members. Admittedly this distribution is an incomplete portion of the family population, and for that reason we do not attempt a serious debiasing effort. We only note the behavior of the detection probability $p(H)$ determined for the phase 2 operations of CSS (bottom panel of Fig. 13). Martes-family orbits have the largest eccentricity among our sample, and this produces the largest stretch of H values in which $p(H)$ decreases from 1 to 0. At magnitude $H \simeq 20$ we have $p \simeq 0.1$.

Taken at a face value, we would infer a large population of small members in the Martes family, such that every one of the three may represent in fact $\simeq 1/p \simeq 10$ asteroids. This logic might be flawed, however, because the three small members were not detected by phase 2 CSS. Strictly speaking, we should not use them to infer anything about Martes family magnitude distribution. Nevertheless, we believe our inferences may be close to reality. This is because all three smallest asteroids in the Martes family were detected by G96/CSS in September 2022. This time period is technically out of the phase 2 interval, but only by a small amount. It also shows the capability of G96 to detect them. The size of the Martes population at $H \simeq 20$ is left for future work.

3.3. Starving young asteroid families with only three known members and asteroid pairs

Lucascavin. This very tight cluster of three asteroids was discovered by Nesvorný & Vokrouhlický (2006), who also

[5] All three of them were pre-covered on CCD images taken by Pan-STARRS in 2011, and also detected in 2014 by a 4-m *Victor M. Blanco* telescope on Cerro Tololo, using the Dark Energy Camera, which can reach much fainter objects than the 1.5-m G96 telescope.

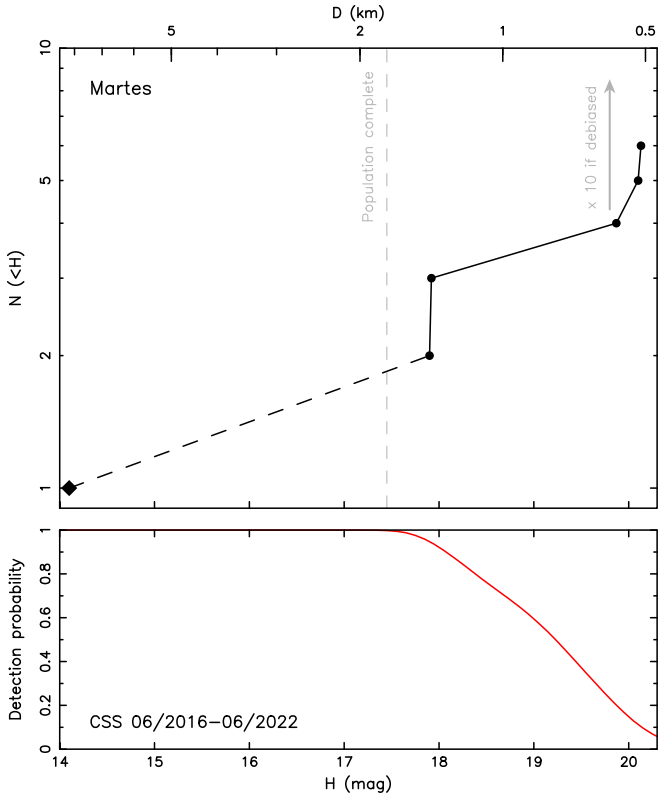

Fig. 13. Top panel: cumulative magnitude distribution $N(< H)$ of the Martes family members. The black symbols are all 6 known members (including the largest asteroid (5026) Martes shown by the diamond). The top abscissa indicates an approximate size computed from H with an assumption of $p_V = 0.06$ value of the geometric albedo (conforming the Ch-class taxonomy). Bottom panel: detection probability $p(H)$ of Martes members as a function of H during the phase 2 operations of CSS based on analysis of geometric and photometric detection factors run on a large synthetic population of Martes members. We find that $p = 1$ up to $H \simeq 17.5$ magnitude, which sets the limit where the Martes population is complete (dashed line on the upper panel). Beyond this limit p decreases to zero at about 20.5 magnitude. At magnitude $\simeq$20 $p \simeq 0.1$. This implies that the three very small members recently detected must represent a tiny sample of a much larger population having about the same size.

estimated its age to 300–800 kyr (the large uncertainty is due to small size of the two small members – see Table A.7 – and unconstrained magnitude of the thermal accelerations in their orbit). A decade later, Pravec et al. (2018) found the three original members were still the only ones in this cluster. They also calculated its age to be between 500 and 1000 kyr using a different method. Assuming the population is complete, these authors also argued that the estimated sizes of the Lucascavin members, and the $\simeq$5.79 h rotation period, might be enough for rotation fission of the parent object to explain their origin (e.g., Pravec et al. 2010, 2019). The difference with respect to the population of pairs is that the assumption that the secondary, escaping from the primary after the fission event, would split into two components (namely the two small members (180255) 2003 VM9 and (209570) 2004 XL40). This possibility was theoretically predicted by Jacobson & Scheeres (2011). If, however, numerous smaller fragments are found in the Lucascavin family, this scenario would become less plausible. Therefore, unlike our study of other clusters in this paper, the goal of our analysis here is to "disprove" the existence of further fragments in the family. Obviously, we cannot meet this goal in an absolute manner, but we can set a lower limit on the absolute magnitude of a putative companion (or, in other words, an upper limit on its size).

Moving towards that goal, we note that all three known members in the Lucascavin family were detected during both phases 1 and 2 of the CSS operations (in our notation, we thus have $N_{obs} = 3$ and $N_{CSS} = 3$)[6]. In order to use as much information as possible, we have combined data from both phases of the CSS operations. Given their different performance, we consider both phases as independent (and uncorrelated) sources of information. Denoting then the detection probability during the phase 1 by p_1, and similarly the detection probability during the phase 2 by p_2, the combined total detection probability p during both phases is

$$p = 1 - (1 - p_1)(1 - p_2). \quad (1)$$

Note that we first characterized the non-detection during both phases (the second term), and then take the complement to unity, which expresses detection in at least one of the CSS phases. Results are shown in Fig. 14.

We first briefly comment on the behavior of p_1 and p_2 (the blue and red curves). The interesting, and at the first sight puzzling, feature of p_1 is that it does not reach a value of 1 even for rather bright objects (its maximum value is only about 0.9). This is not a mistake, but the result of the Lucascavin cluster's semimajor axis. The synodic period of its motion with respect to an Earth observer is in an approximate 7:5 resonance over a year. As a result, for a survey spanning only a short period of time (such as little more than 3 yr of our CSS phase 1 operations), it may happen that Lucascavin objects with certain values of mean longitude in orbit λ never occur in the field-of-view (reasonable solar elongations on the night sky). Since this is a purely geometrical effect, it affects the detection probability of even very bright objects (see, e.g., Tricarico 2017, Fig. 2 for illustration of this effect for near-Earth object characterization). As the duration of the survey extends, this effect minimizes and even disappears. As a result, p_2 in the 6 yr interval of CSS phase 2 (red curve) does not suffer from this problem. The overall detection probability p_1 is smaller than p_2, but both reach $p_1 \simeq p_2 \simeq 0$ at similar $H \simeq 20.5$. This outcome is because the apparent magnitude detection limit is similar for both phases.

Following the trend of the black curve of Fig. 14, $p(H)$, we note that $p(H) \simeq 1$ up to $H \simeq 18.3$. Therefore the Lucascavin population is complete to this magnitude limit. This calculation is a conservative estimate because observations of other surveys may push this limit to higher values. The limit is about one magnitude larger than that of the two small members in the Lucascavin family ($\simeq$17.25). Our result may be therefore interpreted in two ways: either (i) it sets a constraint on Lucascavin family magnitude distribution, or (ii) it starts tracing the population void beyond the known set. The former case would imply at least a magnitude gap between the third and the fourth largest members in the family (this is not impossible, see, e.g., Fig. 2). The latter case may support the idea that the Lucascavin family formed by rotation fission, with the secondary disrupting into two pieces.

Rheinland and Kurpfalz. The pair of asteroids composed of a primary (6070) Rheinland and a secondary (54827) Kurpfalz is the best studied archetype in its class. This is because the

[6] The smaller members, (180255) 2003 VM9 and (209570) 2004 XL40, were detected only 1 and 4 times during the phase 1, though.

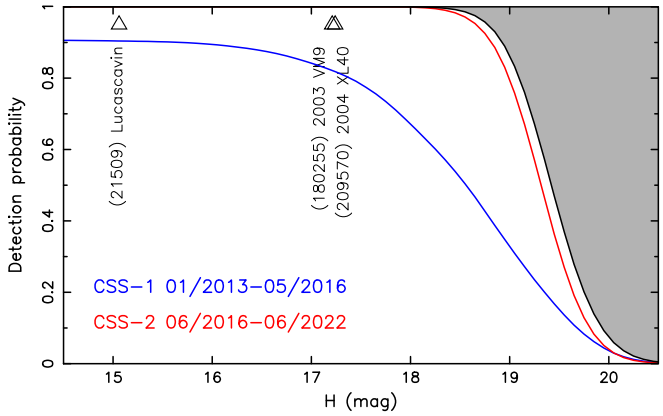

Fig. 14. Detection probability of an additional small fragment in the Lucascavin family: (i) the blue curve is p_1 during the phase 1 of CSS operations, and (ii) the red curve is p_2 during the phase 2 of CSS operations. The black curve is the combined probability p during both phases (Eq. (1)). The gray area allows the existence of an additional small body in the system, whose maximum probability of occurrence is complementary value to the probability p on the left ordinate.

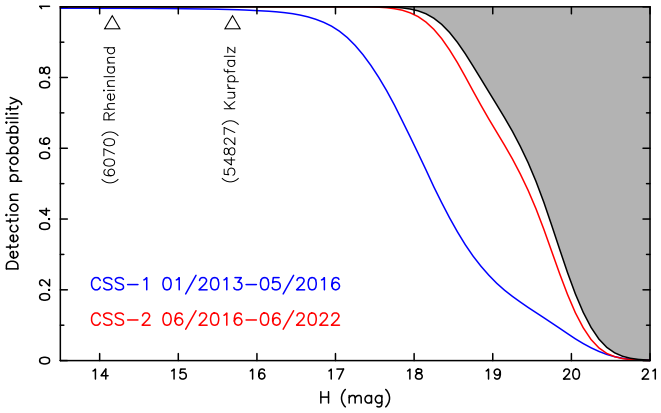

Fig. 15. Detection probability of a companion to Rheinland and Kurpfalz on their heliocentric orbit: (i) the blue curve is p_1 during the phase 1 of CSS operations, and (ii) the red curve is p_2 during the phase 2 of CSS operations. The black curve is the combined probability p during both phases (Eq. (1)). The gray area allows the existence of an additional small body in the system, whose maximum probability of occurrence is complementary value to the probability p on the left ordinate.

two asteroids are rather large, namely the $D_1 \simeq 4.4 \pm 0.6$ km size primary and the $D_2 \simeq 2.2 \pm 0.3$ km size secondary (absolute magnitudes $H_1 = 14.17 \pm 0.07$ and $H_2 = 15.69 \pm 0.04$), and reside in the inner part of the asteroid belt. Their discoveries in 1991 and 2001, and prediscovery data extending to 1950 and 1991, imply a wealth of astrometric observations allowing accurate orbit determination. This has been noticed already by Vokrouhlický & Nesvorný (2008), who used this pair to demonstrate they could reach full convergence in Cartesian space of the two orbits in the past. From this result, they determined the pair had an age of ≃17 kyr. Later, Vokrouhlický et al. (2011, 2017b) conducted photometric observations of both asteroids with the goal to determine their rotation state, including pole orientation, and shape model. Intriguingly, the spin orientation at the likely moment of their formation has not been found to be parallel for the two components, but instead is slightly tilted by about 38°. The well confined spin state for both components in this pair allowed them to pin down the formation epoch to 16.34 ± 0.04 kyr (see Vokrouhlický et al. 2017b). An interesting clue about the formation process, fission of a critically rotating parent body (e.g., Pravec et al. 2010, 2019), is also provided by spectroscopic observations of Rheinland and Kurpfalz: while the first has been found a typical S-class object, the taxonomy of the latter is either Sq- or even Q-class (see Polishook et al. 2014).

Similarly to the case of the Lucascavin family, we aim to determine the magnitude limit for nonexistence of a putative companion fragment following Rheinland and Kurpfalz on their heliocentric orbit. Since both Rheinland and Kurpfalz were detected during CSS phases 1 and 2, we may again combine detection probabilities p_1 and p_2 to obtain the total probability p according to the formula (1). Results are shown in Fig. 15.

In this case, p_1 is comfortably close to unity even for the fainter component (54827) Kurpfalz[7]. However, p_1 starts dropping to zero right after H_2 of the secondary, such that limited useful information would have been reached if we only had the phase 1 data. Luckily, the power of the CSS phase 2 observations make extending the final detection probability p for the orbits in this pair to unity, even near $H \simeq 18$. We may thus conclude that the available observations rule out a companion fragment of this pair to this limit, which is $\Delta H \simeq 2.3$ larger than H_2 of the secondary. Assuming the same albedo, the hypothetical companion – if it exists – must have a size smaller than $\simeq 10^{-0.2\Delta H} D_2 \simeq 0.8$ km.

[7] In fact, (6070) Rheinland has been detected 8 and 26 times during the phases 1 and 2, while (54827) Kurpfalz has been detected 8 and 21 times the phases 1 and 2.

4. Results

We now proceed towards a more advanced debiasing method than previously used in the case of the Wasserburg family. The four families introduced in Sect. 3.1 with large-enough known population of members – Datura, Adelaide, Rampo and Hobson – will serve us as our testbed cases.

The method, in essence similar to what has been used by Vokrouhlický et al. (2017a), goes as follows:

- First, we consider the CSS phase 2 detected sample $\{H_i^{\rm o}\}$ $(i = 1, \ldots, N_{\rm CSS})$ of the family asteroids and we select a certain member $H_j^{\rm o}$ for which $p(H_j^{\rm o}) \simeq 1$ (we call it a "branching point"). We assume that the population is complete up to the absolute magnitude of that member and becomes incomplete for magnitudes larger than $H_j^{\rm o}$. The cumulative magnitude distribution is therefore represented by the observed population until $H_j^{\rm o}$, where it has N_1 members, and then continued with a synthetic (model) population as described below. We also denote the number of family members with magnitudes $\geq H_j^{\rm o}$ detected during the CSS phase 2 by $N'_{\rm CSS} (\leq N_{\rm CSS})$.
- Second, we generated the total synthetic population of family members $\{H_i^{\rm s}\}$ having absolute magnitudes in between $H_1 = H_1^{\rm s} = H_j^{\rm o}$ and a certain value H_2 sufficiently larger than $H_{N_{\rm CSS}}^{\rm o}$ with a statistical distribution of the tested magnitude distribution function (we use the sequence of $\mathcal{M}$ models described below and always order the magnitude sequence from the smallest to the largest).
- Third, we used the detection probability $p(H)$ of the CSS observations to transform the total synthetic population to the biased synthetic population $\{H_i^{\rm b}\}$, such that each of $\{H_i^{\rm s}\}$ is consulted as to its detectability. In practice, for each $H_i^{\rm s}$

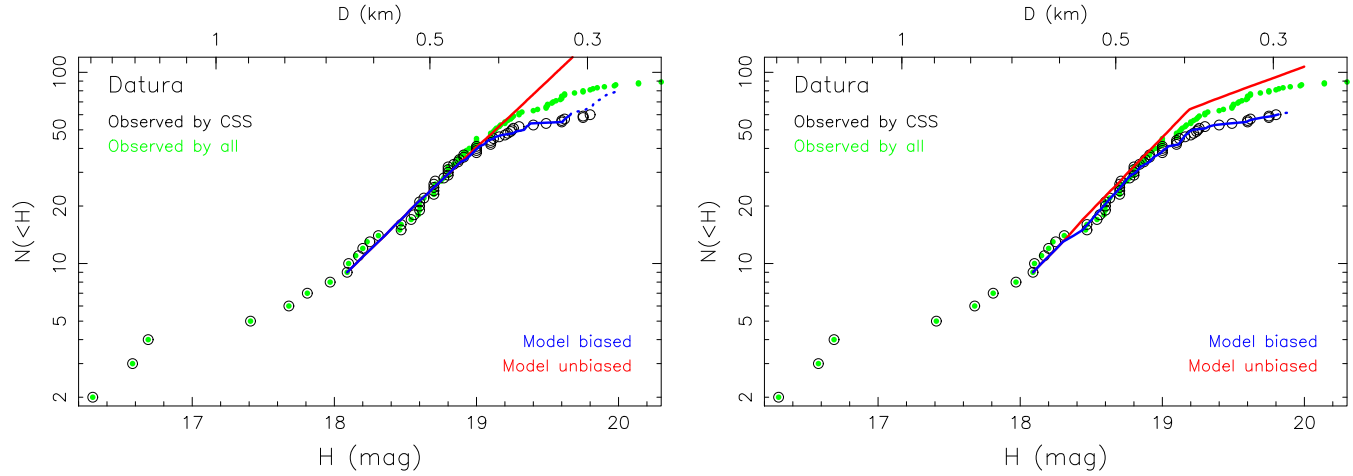

Fig. 16. Best-fit solution of the complete Datura population to the magnitude limit $H_2 = 20$ and its comparison to the observed population. Left panel: the single power law $\mathcal{M}1$ model with the free parameter representing the slope γ. The best fit value is $\gamma = 0.70$, and the corresponding $\chi^2_{\rm min} = 13.36$. Right panel: The broken power-law model $\mathcal{M}2$ with three adjustable parameters $(H_{\rm break}, \gamma_1, \gamma_2)$. The best-fit values (red star in Fig. 17) are: $H_{\rm break} = 19.13$, $\gamma_1 = 0.75$, and $\gamma_2 = 0.31$, and the corresponding $\chi^2_{\rm min} = 3.85$. The green symbols are the currently known population of Datura family members from all surveys, the open black circles are the members detected during the phase 2 of CSS ($\{H^{\rm o}_i\}$). The red line is the complete model ($\{H^{\rm s}_i\}$), the blue line is the biased model ($\{H^{\rm b}_i\}$; the solid part of the blue line has $N'_{\rm CSS}$ objects, the same as the number of detected objects beyond the branching magnitude $H^{\rm o}_j$, the dotted part is the continuation of the biased population not used for the least-squares fitting in Eq. (2)). The upper abscissa shows an estimate of the size for the geometric albedo value $p_{\rm V} = 0.24$.

we evaluated $p(H^{\rm s}_i)$ and compared it to a uniformly random number r between 0 and 1, providing a rationale for detectability or non-detectability: (i) if $r \le p(H^{\rm s}_i)$, the asteroid is deemed detected and we record $\{H^{\rm s}_i\}$ in the $\{H^{\rm b}_i\}$ sequence, and (ii) if $r > p(H^{\rm s}_i)$, the asteroid is deemed not detected and we proceed to the next $\{H^{\rm s}_i\}$ value.

– Fourth, we evaluated a chi-square type target function

$$\chi^2 = \sum_{i=1}^{N'_{\rm CSS}} \left(\frac{H^{\rm b}_i - H^{\rm o}_{j+i-1}}{\sigma_i} \right)^2 , \qquad (2)$$

comparing the modeled and biased magnitude distribution to the detected set $\{H^{\rm o}_i\}$ by CSS beyond the branching magnitude $H^{\rm o}_j$.

For sake of simplicity, we (i) use $\sigma_i = 0.1$ magnitude for all bodies, and (ii) adopt Gaussian statistics to judge the goodness-of-the-fit and set confidence limits on the adjusted parameters of the model needed to construct the complete (not-biased) synthetic population $\{H^{\rm s}_i\}$. As for the synthetic population, we use the following sequence of power-law models:

– Model $\mathcal{M}1$ – a straight single-slope power law $N(< H) \propto 10^{\gamma H}$ with one adjustable parameter γ (the absolute normalization for all $\mathcal{M}$-models is set by number $N_1 = N(< H_1)$ of family asteroids at H_1, because we make sure that the population is complete to that limit);
– Model $\mathcal{M}2$ – a broken power-law model with one adjustable break-point at $H_{\rm break}$ ($H_1 \le H_{\rm break} \le H_2$) and two adjustable slope exponents γ_1 and γ_2 for H values in the intervals $(H_1, H_{\rm break})$ and $(H_{\rm break}, H_2)$ respectively;
– Model $\mathcal{M}3$ – a broken power-law model with two adjustable break-points at $H_{\rm break,1}$ and $H_{\rm break,2}$ ($H_1 \le H_{\rm break,1} < H_{\rm break,2} \le H_2$) and three adjustable slope exponents γ_1, γ_2 and γ_3 for H values in the intervals $(H_1, H_{\rm break,1})$, $(H_{\rm break,1}, H_{\rm break,2})$ and $(H_{\rm break,2}, H_2)$ respectively;

and similarly for $\mathcal{M}i$ model with $2i - 1$ parameters ($i - 1$ break-points and i slopes for the intermediate intervals of H). In practice, we limit ourselves to $\mathcal{M}3$ at maximum in this paper.

Denote $\mathbf{p}$ the set of model parameters (e.g., $\mathbf{p} = (H_{\rm break}, \gamma_1, \gamma_2)$ for the $\mathcal{M}2$ model). Since $\chi^2 = \chi^2(\mathbf{p})$ in (2), the usual goal is to minimize its value by selecting the best-fit $\mathbf{p}_\star$ parameter choice. We use a simple Monte Carlo sampling of $\mathbf{p}$ space to find these values and to map χ^2 behavior within some zone about the minimum value $\chi^2_{\rm min} = \chi^2(\mathbf{p}_\star)$. The confidence limits on $\mathbf{p}$ are found by choosing a certain domain with a threshold $\chi^2 = \chi^2_{\rm min} + \Delta\chi^2$. For instance, the 99% confidence limit in one, three and five parametric degrees of freedom in $\mathcal{M}1$, $\mathcal{M}2$ and $\mathcal{M}3$ models corresponds to $\Delta\chi^2 = 6.63$, 11.3 and 15.1 respectively (e.g., Press et al. 2007). Similarly the measure of the goodness-of-fit is judged from the $\chi^2_{\rm min}$ value using the incomplete gamma function as discussed in Press et al. (2007).

Datura. Considering the data in Fig. 1 we chose $j = 9$ in the case of the Datura family, namely taking the absolute magnitude $H^{\rm o}_j = 18.09$ of the ninth family member as the branching point (i.e., $N'_{\rm CSS} = 52$ in this case). We will test the $\mathcal{M}1$ and $\mathcal{M}2$ models[8].

In the former case, we find $\gamma = 0.70^{+0.03}_{-0.02}$ (99% confidence level) and the best-fit solution having $\chi^2_{\rm min} = 13.36$. In the latter case, we find $H_{\rm break} = 19.13^{+0.37}_{-0.48}$, $\gamma_1 = 0.75^{+0.15}_{-0.09}$, and $\gamma_2 = 0.31^{+0.30}_{-0.25}$ (99% confidence level) and the best-fit solution having a significantly improved $\chi^2_{\rm min} = 3.85$ (the improvement for the $\mathcal{M}3$ model is already statistically insignificant).

The best-fit solutions of both models are shown in Fig. 16. While formally the minimum $\chi^2_{\rm min}$ values are both statistically justifiable using the Q-function measure (Press et al. 2007), the $\mathcal{M}1$ performs quite worse beyond $H \simeq 19.5$. This is because continuing the steep power-law distribution required by the

[8] Results discussed in this section do not include (429988) 2013 PZ36 among the family members. However, our tests showed that they are robust. By including this body, we observe only a statistically insignificant change of the solution, the largest for $\gamma_1 = 0.70^{+0.15}_{-0.09}$ parameter of the $\mathcal{M}2$ model.

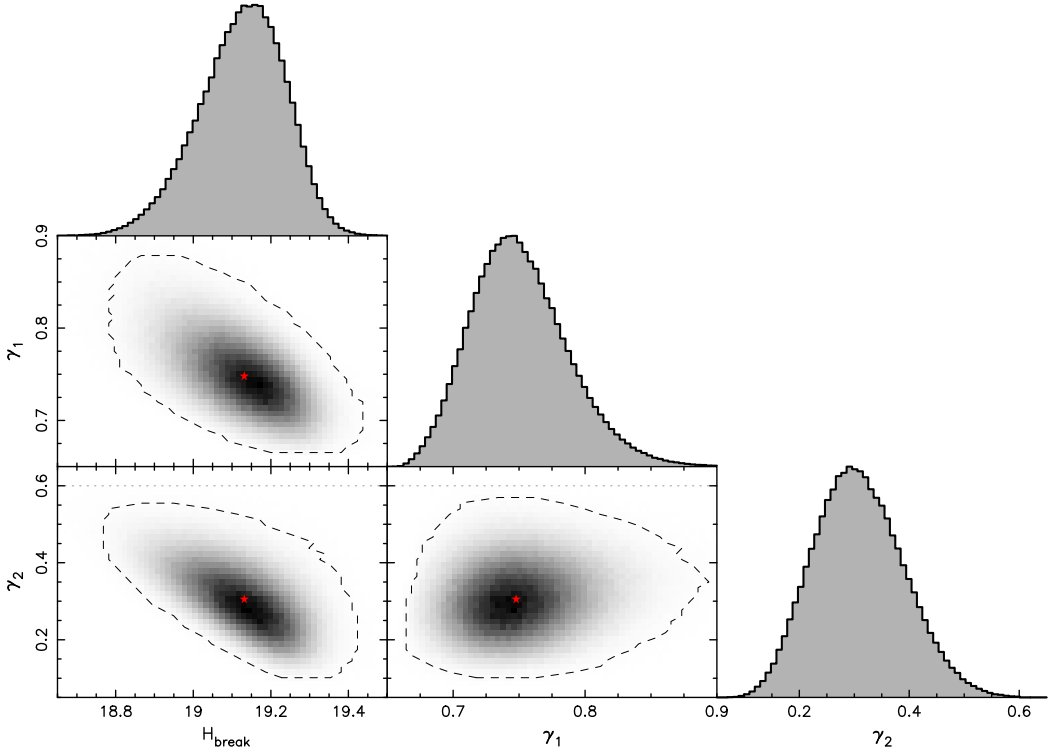

Fig. 17. Admissible parameter values of the $\mathcal{M}2$ broken power-law model approximating Datura family absolute magnitude distribution in the range $H \in (H_1, H_2) = (18.09, 20)$. There are three solved-for parameters in the model: (i) the break-point magnitude $H_{\rm break}$, (ii) the power-law exponent γ_1 for $H \le H_{\rm break}$, and (iii) the power-law exponent γ_2 for $H \ge H_{\rm break}$. Each of the panels shows a projection of the solution onto different 2D subspaces of the 3D space of parameters $(H_{\rm break}, \gamma_1, \gamma_2)$. The dashed line delimits 99% confidence limit zone of the solution, and the gray-scale is proportional to the probability density distribution of the solutions. The best-fit parameter combination is shown by red star symbol. The gray histograms are simply 1D probability density distributions for each of the parameters on the abscissa. The dotted line at γ_1 or γ_2 values of 0.6 is shown for reference.

magnitude distribution of the Datura members between $H = 18$ and 19 would keep pushing the detactable population high (given the only slow decay of the detection probability $p(H)$ from Fig. 1). This problem is remedied by setting a break-point at which the distribution becomes shallower; this behavior is readily provided by the $\mathcal{M}2$ model. The upper abscissa on both panels of Fig. 16 is an estimate of Datura member size using the geometric albedo value $p_{\rm V} = 0.24$. The break-point magnitude $H_{\rm break}$ solution within the $\mathcal{M}2$ model maps onto a 0.3–0.5 km range of sizes.

Figure 17 provides more detailed information on the $\mathcal{M}2$ model parameter solution. In spite of weak correlations, the solution seems to be well-behaved. Interestingly, the slope exponents satisfy $\gamma_1 > 0.6$ and $\gamma_2 < 0.6$. The magnitude slope γ translates to an exponent $\alpha = -5\gamma$ of a cumulative size distribution (assuming constant albedo on a given interval of H-values). Therefore the threshold value 0.6 maps onto a critical size exponent -3: for shallower distributions the mass is dominated by the largest members, while for steeper distributions the mass is dominated by the smallest fragments.

In our $\mathcal{M}2$ solution for Datura members, the mass is dominated by the sizes at the breakpoint, while in the $\mathcal{M}1$ solution the fragment mass cannot be well constrained because it is dominated by the smallest members. Here we use the $\mathcal{M}2$ solution and estimate the total mass $m_{\rm frag}$ contained in Datura family members with absolute magnitudes between 16 and 20 from our complete model (i.e., excluding (1270) Datura itself). We also normalize $m_{\rm frag}$ by the mass $m_{\rm LF}$ of (1270) Datura. The statistical distribution of this ratio, as mapped from the 99% confidence level parametric region shown in Fig. 17, is shown in

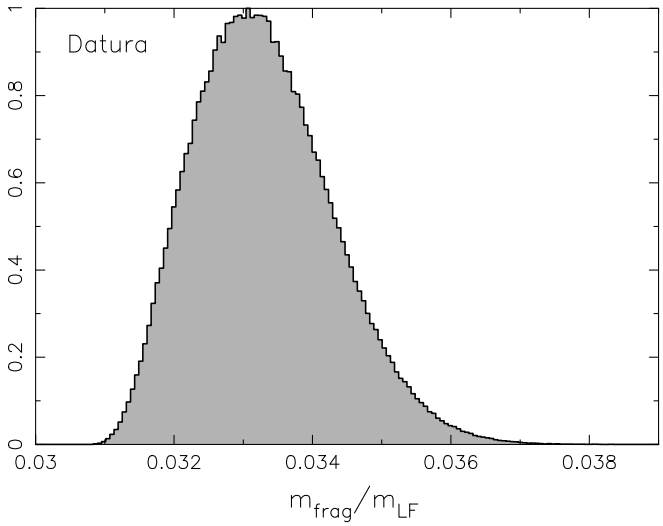

Fig. 18. Probability density distribution of the ratio $m_{\rm frag}/m_{\rm LF}$ (normalized to unit at maximum), where $m_{\rm frag}$ is the mass/volume of all members up to absolute magnitude 20 without (1270) Datura, and $m_{\rm LF}$ is the mass/volume of the largest member (1270) Datura. Solution using the broken power-law model $\mathcal{M}2$.

Fig. 18. We find $m_{\rm frag}/m_{\rm LF} = 0.033^{+0.005}_{-0.002}$. Unless the cumulative number of Datura members becomes significantly steeper somewhere beyond the magnitude limit 20, which is certainly possible (e.g., Durda et al. 2007), we estimate that their collective mass only represents ≃3.3% of the (1270) Datura mass. From this

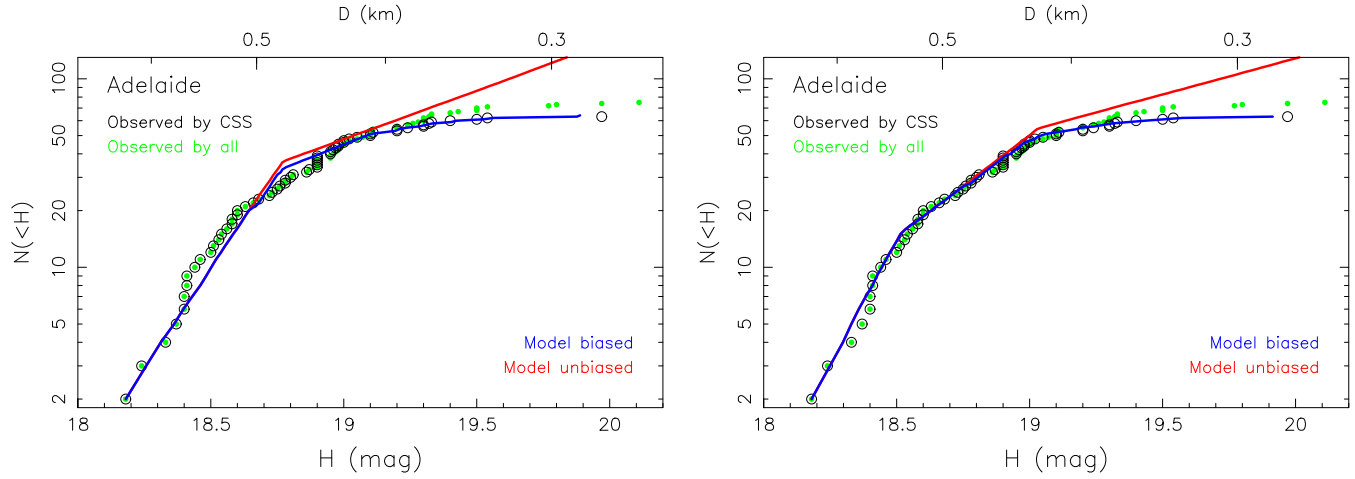

Fig. 19. Best-fit solution of the complete Adelaide population to the magnitude limit $H = 20$ and its comparison to the observed population. Left panel: the broken power-law model $\mathcal{M}2$ with three adjustable parameters ($H_{\rm break}, \gamma_1, \gamma_2$). The best-fit values (red star in Fig. 20) are: $H_{\rm break} = 18.78$, $\gamma_1 = 2.08$, and $\gamma_2 = 0.47$, and the corresponding $\chi^2_{\rm min} = 12.18$. Right panel: the broken power-law model $\mathcal{M}3$ with five adjustable parameters ($H_{\rm break,1}, H_{\rm break,2}, \gamma_1, \gamma_2, \gamma_3$). The best-fit values are: $H_{\rm break,1} = 18.57$, $H_{\rm break,2} = 19.04$, $\gamma_1 = 2.41$, $\gamma_2 = 1.00$, and $\gamma_3 = 0.34$, and the corresponding $\chi^2_{\rm min} = 3.77$. The green symbols are the currently known population of Adelaide family members from all surveys, the open black circles are the members detected during the phase 2 of CSS ($\{H^{\rm o}_i\}$). The red line is the complete model ($\{H^{\rm s}_i\}$), the blue line is the biased model ($\{H^{\rm b}_i\}$; the solid part of the blue line has $N'_{\rm CSS}$ objects, the same as the number of detected objects beyond the branching magnitude $H^{\rm o}_j$, the dotted part is the continuation of the biased population not used for the least-squares fitting in Eq. (2)).

analysis, we suggest the family may have been formed from a large cratering event.

Adelaide. The extreme nature of the magnitude distribution in the Adelaide family (Fig. 4) makes us choose $j = 2$, therefore we associate the point to the first member next to (525) Adelaide with $H^{\rm o}_j = 18.18$. With that choice we have $N'_{\rm CSS} = 62$. In this case, we test $\mathcal{M}1$, $\mathcal{M}2$ and $\mathcal{M}3$ models.

We find that the single power-law model $\mathcal{M}1$ is incompatible with the family data. The formally best-fit slope $\gamma \simeq 1.86$ tries to compromise between the extremely steep part of the magnitude distribution between 18.18 and ≃18.75 and much shallower distribution beyond. However, none of the features is matched well and the formal $\chi^2_{\rm min} \simeq 235$ has to be statistically rejected. The basic inconsistency of such a model stems from the behavior of the detection probability $p(H)$ shown in the bottom panel of Fig. 4. In simple words, $p(H)$ is quite smooth and gradual even beyond ≃19 magnitude and does not resemble the sharp lack of detected fragments at ≃18.7 magnitude. In the Adelaide family case, we need some slope change even in the complete population, and this is provided by models $\mathcal{M}2$ and $\mathcal{M}3$.

In the former case, we find $H_{\rm break} = 18.78^{+0.14}_{-0.26}$, $\gamma_1 = 2.08^{+0.92}_{-0.19}$, and $\gamma_2 = 0.47^{+0.30}_{-0.24}$ (99% confidence level). The best-fit solution has $\chi^2_{\rm min} = 12.18$. The model reflects a slope change from steep to shallow near 18.75. The minimum of χ^2 reached in the $\mathcal{M}2$ model is fully acceptable, yet the left panel on Fig. 19 indicates the solution may still be improved (obviously at the expense of more parameters). This is provided by the $\mathcal{M}3$ model (the right panel on Fig. 19), which has $H_{\rm break,1} = 18.57^{+0.29}_{-0.26}$, $H_{\rm break,2} = 19.04^{+1.00}_{-0.14}$, $\gamma_1 = 2.41^{+0.67}_{-0.48}$, $\gamma_2 = 1.00^{+0.77}_{-0.59}$, and $\gamma_3 = 0.34^{+0.44}_{-0.28}$ (99% confidence level) and has $\chi^2_{\rm min} = 3.77$.

Figure 20 shows 2D projections of the $\mathcal{M}2$ model parameters, resembling those for Datura family in Fig. 17, except for γ_1 value significantly steeper. The $\mathcal{M}3$ model parameters are more correlated within each other, as many combinations for positions of the two breakpoints $H_{\rm break,1}$ and $H_{\rm break,2}$ and the intermediate slopes γ_1 and γ_2, are possible. Obviously, the solution of the faintest-slope γ_3 is consistently shallow, even shallower than γ_2 in model $\mathcal{M}2$ (see Fig. 20).

There is a robust, common result following from the $\mathcal{M}2$ and $\mathcal{M}3$ models: (i) the initial slope parameter in the 18.2–18.6 absolute magnitude range must be very steep (i.e., 2–3, and (ii) the final slope beyond absolute magnitude 19 must be rather shallow (i.e., 0.1–0.7). Given the shallow magnitude distribution at the limit of very small Adelaide members (for most part < 0.6), the bias-corrected fragment population mass is dominated by $H \simeq 19$ Adelaide members. We can thus repeat the computation performed for the Datura family, and compute the ratio $m_{\rm frag}/m_{\rm LF}$ of the Adelaide members with $H > 18$ ($m_{\rm frag}$) and the mass of the largest asteroid (525) Adelaide itself ($m_{\rm LF}$). Obviously, we carry out this computation for the bias-corrected populations of the $\mathcal{M}2$ and $\mathcal{M}3$ models, rather than the observed population of the Adelaide family members.

The results, shown in Fig. 21, provide tight constraints on the complete population of the Adelaide members in the 18–20 magnitude range: $m_{\rm frag}/m_{\rm LF} = 0.0088^{+0.0013}_{-0.0009}$ for the $\mathcal{M}2$ model, and $m_{\rm frag}/m_{\rm LF} = 0.0084^{+0.0003}_{-0.0005}$ for the $\mathcal{M}3$ model. If these estimates hold also for the population at the family origin (see Sect. 5 for an alternative option), the Adelaide family is an exemplary case of a large cratering event. We estimated the size of the expected crater on (525) Adelaide in Sect. 5.

Rampo. In this case, we use $j = 4$, corresponding to a $H^{\rm o}_j = 18.09$ magnitude branching point (Fig. 10). Using that choice we have $N'_{\rm CSS} = 22$, slightly less data than for the Datura and Adelaide families. We tested the $\mathcal{M}1$ and $\mathcal{M}2$ models in this situation.

The best-fit with a single power-law $\mathcal{M}1$ model only reaches $\chi^2_{\rm min} = 31.4$ (with the median slope parameter $\gamma \simeq 1.44$). Given $N'_{\rm CSS} = 22$ data points, this solution is statistically unacceptable (the quality factor $Q \simeq 0.067$; see Press et al. 2007). Figure 22 illustrates the problem in a graphical way, namely the predicted population of fragments beyond magnitude 19 (blue dashed line on the left panel) becomes steep and incompatible with the single Rampo fragment detected by CSS. Things improve if the magnitude of the power-law model $\mathcal{M}1$ is shifted to $H^{\rm o}_j = 18.0$

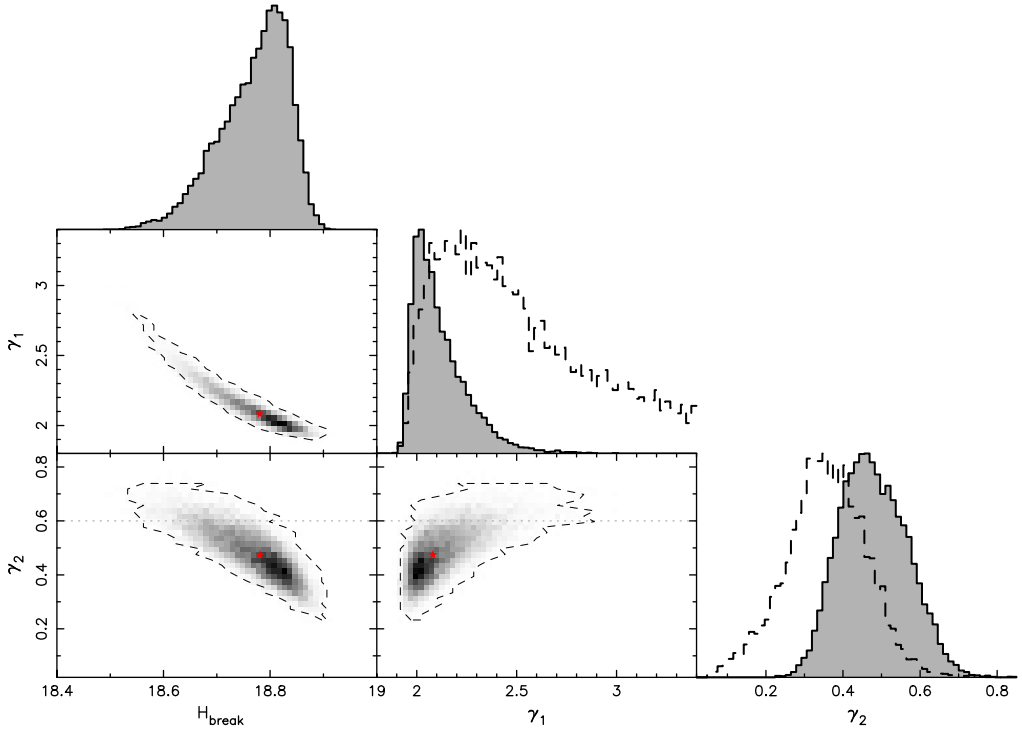

Fig. 20. Admissible parameter values of a $\mathcal{M}2$ broken power-law model approximating Adelaide family absolute magnitude distribution in the range $H \in (H_1, H_2) = (18.2, 20)$. There are three solved-for parameters in the model: (i) the break-point magnitude $H_{\rm break}$, (ii) the power-law exponent γ_1 for $H \le H_{\rm break}$, and (iii) the power-law exponent γ_2 for $H \ge H_{\rm break}$. Each of the panels shows a projection of the solution onto different 2D subspaces of the 3D space of parameters $(H_{\rm break}, \gamma_1, \gamma_2)$. The dashed line delimits 99% confidence limit zone of the solution, and the gray-scale is proportional to the probability density distribution of the solutions. The best-fit parameter combination is shown by red star symbol. The gray histograms are simply 1D probability density distributions for each of the parameters on the abscissa; the dashed histograms along the distributions of the γ_1 and γ_2 exponents correspond to the first and the last exponent in the $\mathcal{M}3$ broken power-low models with two break-points ($H_{\rm break,1}$, $H_{\rm break,2}$; i.e., the first in the interval $(18.2, H_{\rm break,1})$, and the second in the interval $(H_{\rm break,2}, 20)$). The dotted line at γ_1 or γ_2 values of 0.6 is shown for reference.

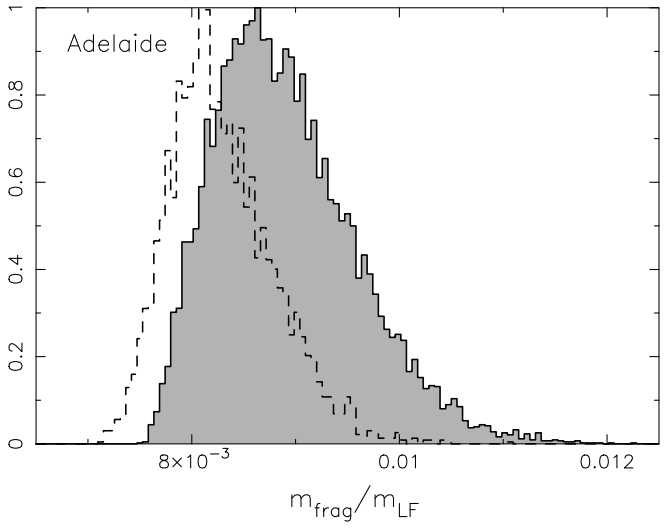

Fig. 21. Probability density distribution of the ratio $m_{\rm frag}/m_{\rm LF}$ (normalized to unit at maximum), where $m_{\rm frag}$ is the mass/volume of all members up to absolute magnitude 20 without (525) Adelaide, and $m_{\rm LF}$ is the mass/volume of the largest asteroid (525) Adelaide. The solid/gray histogram for the $\mathcal{M}2$ model, the dashed histogram for the $\mathcal{M}3$ model (all models whose parameters **p** are within the 99% confidence level of the family population were used).

(still within the assumed 0.1 magnitude uncertainty). This helps to straighten the sequence of observed members immediately after $H_j^{\rm o}$, where the detection probability is still close to 1. With that change, the single power-law model $\mathcal{M}1$ provides best match with $\chi^2_{\rm min} = 17.60$ (and, obviously, smaller slope $\gamma \simeq 1.17$). While not impressive, the solution is formally acceptable, but it suffers from the same problem in matching the faint end of the observed Rampo population using CSS.

The broken power-law model $\mathcal{M}2$ performs much better in this circumstance. It reaches $\chi^2_{\rm min} = 1.52$, and the parameter solution $H_{\rm break} = 18.47^{+0.37}_{-0.28}$, $\gamma_1 = 1.72^{+1.28}_{-0.40}$, and $\gamma_2 = 0.51^{+0.39}_{-0.49}$ (99% confidence level; see Fig. 23). The overall median slope $\simeq$1.17–1.44 is thus traded for a steeper leg initially, followed with a shallower part beyond $H_{\rm break}$. The small $\chi^2_{\rm min}$ conforms to the visually perfect match shown on the right panel of Fig. 22.

Figure 24 shows the model predicted mass in the Rampo members between magnitudes 18 and $\simeq$19.5, namely $m_{\rm frag}/m_{\rm LF} = 0.16^{+0.08}_{-0.02}$. However, since the γ_2 slope beyond $H_{\rm break}$ tends to be steep (with value larger than 0.6 not excluded), the real fragment mass with respect to (10321) Rampo may be even larger. In any case, out of the three families analyzed so far, the Rampo family represents the most energetic collisional event.

Hobson. The record of observed Hobson members, both the total count and the subset detected by CSS, is comparable to the Rampo family. However, because of Hobson's larger

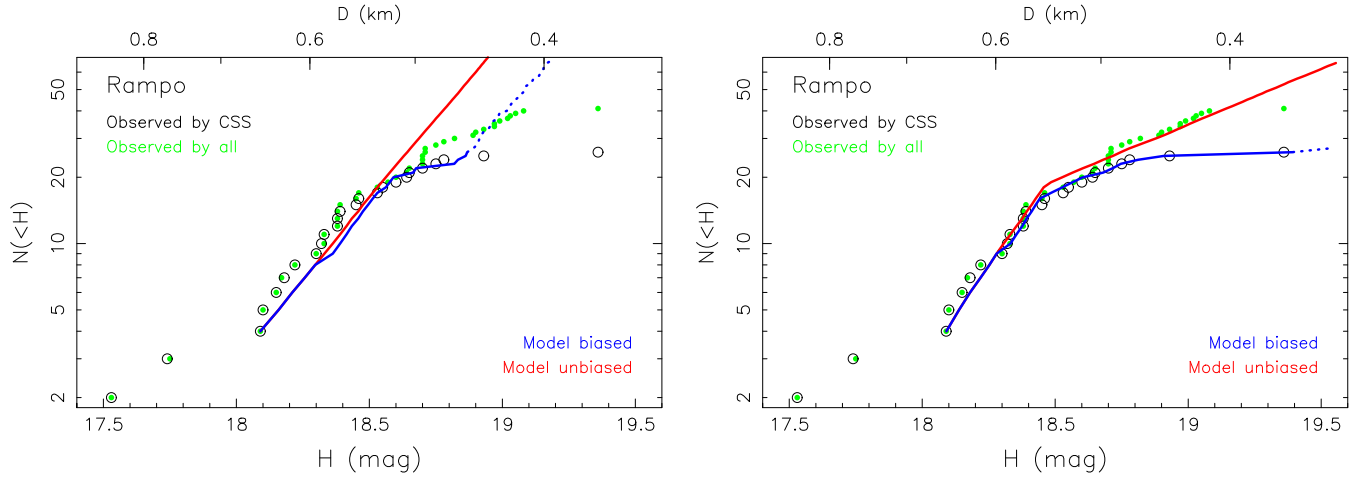

Fig. 22. Best-fit solution of the complete Rampo population to the magnitude limit $H_2 = 20$ and its comparison to the observed population. Left panel: the single power law $\mathcal{M}1$ model with the free parameter representing the slope γ. The best fit value is $\gamma \simeq 1.17$, and the corresponding $\chi^2_{\rm min} = 17.6$. Right panel: The broken power-law model $\mathcal{M}2$ with three adjustable parameters $(H_{\rm break}, \gamma_1, \gamma_2)$. The best-fit values (red star in Fig. 23) are: $H_{\rm break} = 18.47$, $\gamma_1 = 1.72$, and $\gamma_2 = 0.51$, and the corresponding $\chi^2_{\rm min} = 1.25$. The green symbols are the currently known population of Rampo family members from all surveys, the open black circles are the members detected during the phase 2 of CSS ($\{H^{\rm o}_i\}$). The red line is the complete model ($\{H^{\rm s}_i\}$), the blue line is the biased model ($\{H^{\rm b}_i\}$; the solid part of the blue line has $N'_{\rm CSS}$ objects, the same as the number of detected objects beyond the branching magnitude $H^{\rm o}_j$, the dotted part is the continuation of the biased population not used for the least-squares fitting in Eq. (2)). The upper abscissa shows an estimate of the size for the geometric albedo value $p_{\rm V} = 0.24$.

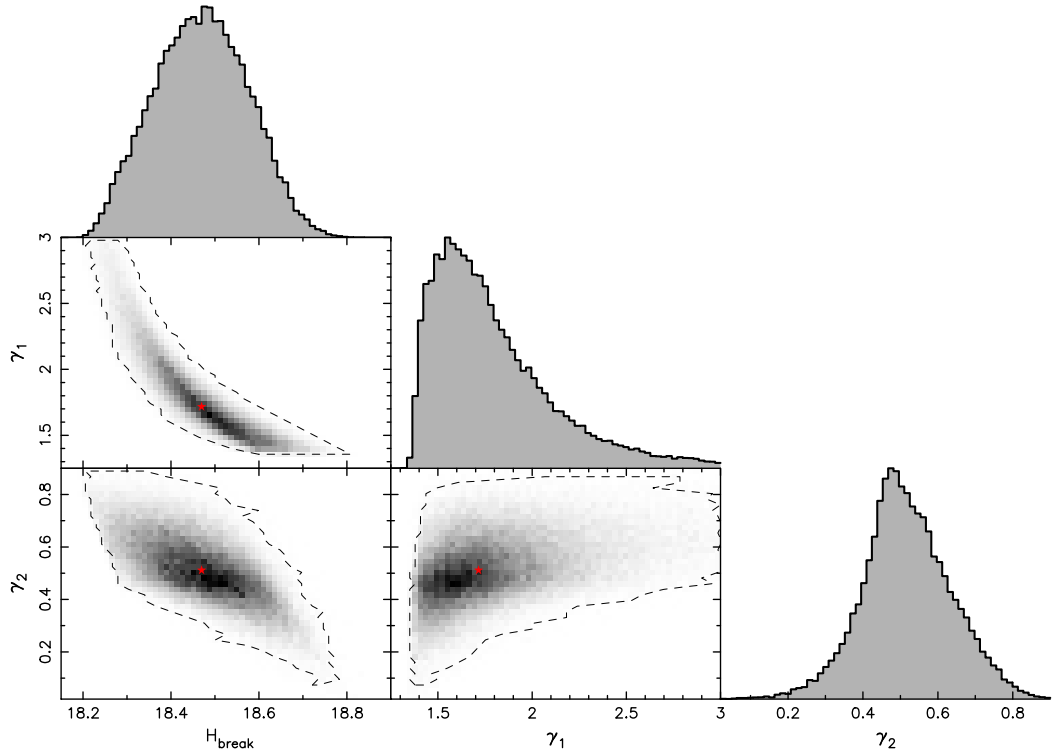

Fig. 23. Admissible parameter values of the $\mathcal{M}2$ broken power-law model approximating Rampo family absolute magnitude distribution in the range $H \in (H_1, H_2) = (18.1, 20)$. There are three solved-for parameters in the model: (i) the break-point magnitude $H_{\rm break}$, (ii) the power-law exponent γ_1 for $H \le H_{\rm break}$, and (iii) the power-law exponent γ_2 for $H \ge H_{\rm break}$. Each of the panels shows a projection of the solution onto different 2D subspaces of the 3D space of parameters $(H_{\rm break}, \gamma_1, \gamma_2)$. The dashed line delimits 99% confidence limit zone of the solution, and the gray-scale is proportional to the probability density distribution of the solutions. The best-fit parameter combination is shown by red star symbol. The gray histograms are simply 1D probability density distributions for each of the parameters on the abscissa. The dotted line at γ_1 or γ_2 values of 0.6 is shown for reference.

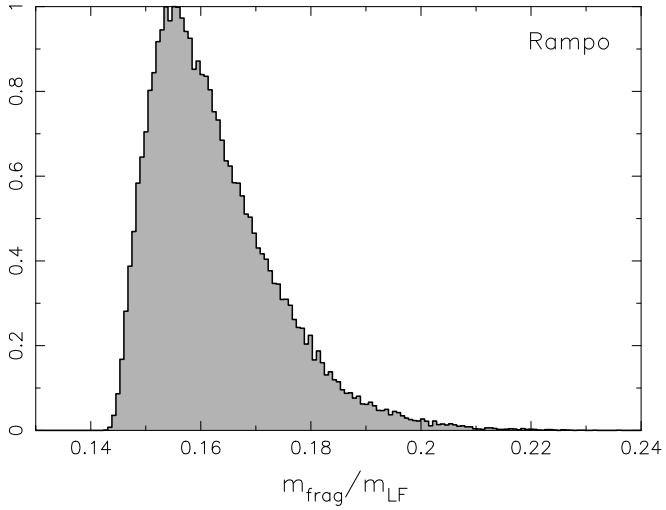

Fig. 24. Probability density distribution of the ratio $m_{\rm frag}/m_{\rm LF}$ (normalized to unit at maximum), where $m_{\rm frag}$ is the mass/volume of all members up to absolute magnitude 20 without (10321) Rampo, and $m_{\rm LF}$ is the mass/volume of the largest asteroid (10321) Rampo. Solution using the broken power-law model $\mathcal{M}2$.

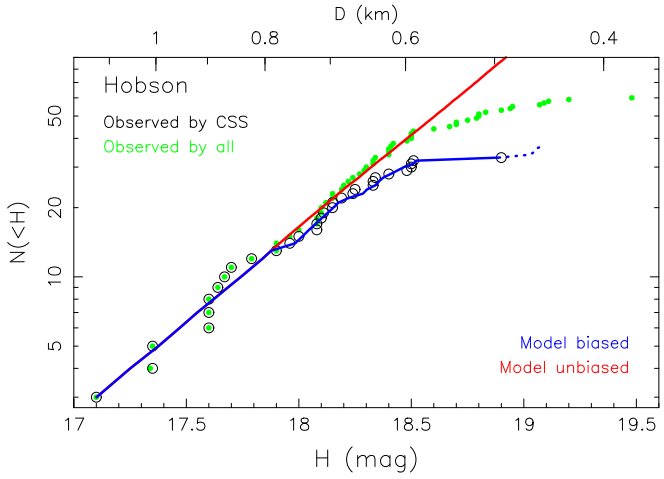

Fig. 25. Best-fit solution of the complete Hobson population to the magnitude limit $H_2 = 19$ and its comparison to the observed population. The single power law $\mathcal{M}1$ model with the free parameter representing the slope γ. The best fit value is $\gamma = 0.81$, and the corresponding $\chi^2_{\rm min} = 6.31$. The green symbols are the currently known population of Hobson family members from all surveys, the open black circles are the members detected during the phase 2 of CSS ($\{H^{\rm o}_i\}$). The red line is the complete model ($\{H^{\rm s}_i\}$), the blue line is the biased model ($\{H^{\rm b}_i\}$; the solid part of the blue line has $N'_{\rm CSS}$ objects, the same as the number of detected objects beyond the branching magnitude $H^{\rm o}_j$, the dotted part is the continuation of the biased population not used for the least-squares fitting in Eq. (2)). The upper abscissa shows an estimate of the size for the geometric albedo value $p_{\rm V} = 0.2$.

heliocentric distance, and its larger eccentricity, the predicted detection probability by CSS is shifted by nearly a magnitude towards small H values (see Figs. 7 and 10). This allows us to conduct the bias-correction on a shifted segment of Hobson member magnitudes/sizes if compared to Rampo, which explains the differences in results.

In this case, we use $j = 3$, corresponding to the $H^{\rm o}_j = 17.10$ magnitude branching point (Fig. 7). Using that choice, we have $N'_{\rm CSS} = 31$. We tested the $\mathcal{M}1$ and $\mathcal{M}2$ models in this situation.

Given the aforementioned difference in detection probabilities for the Rampo and Hobson families, the $\mathcal{M}1$ model is currently sufficient to match the Hobson population between ≃17 and ≃19 magnitudes (Fig. 25). The best-fit simulation reaches $\chi^2_{\rm min} = 6.31$, while the simulations using the $\mathcal{M}2$ model were able to improve this value to $\chi^2_{\rm min} = 5.55$. This is not enough of a statistically significant difference to justify the necessity of a broken power-law model for the Hobson population of members; the simple power-law model performs just as well. The slope parameter is $\gamma = 0.81^{+0.03}_{-0.02}$ (99% confidence level). Because this value is larger than 0.6, we cannot estimate the mass contained in the fragment population, (as the smallest asteroids still dominate the mass). We can only set a lower limit from the population available to us, and this gives $m_{\rm frag}/m_{\rm LF} \geq 0.6$. In this case, $m_{\rm LF}$ contains the mass of the two largest asteroids, (18777) Hobson and (57738) 2001 UZ160. Clearly, the Hobson family results from the catastrophic disruption of a parent body.

5. Discussion and conclusions

Our work provides evidence for a break in the magnitude distribution in several of the very young families analyzed here. Before considering implications, however, we first must attempt to further justify the result and understand its meaning. We can think of at least two conventional reasons for what we see.

Missing halo of small members? The first possibility is that we were unable to identify small family members beyond $H_{\rm break}$. Their deficit, quantitatively as shown by the shallow slope at faint magnitudes, may not be real, but instead represents a failure in our the clustering association. Perhaps, many of these small fragments were ejected with larger velocities and drifted farther from the core of the family. This scenario is a plausible situation for larger and older families in the main belt, which are identified in 3D proper element space by their large spatial densities of asteroids compared to the background population (see discussion in Nesvorný et al. 2015). For the very young families, however, clusters in the 5D space of osculating orbital elements, with additional tracers such as the correlated values of the secular angles Ω and ϖ (Sect. 3), help to minimize the problem of missing members (if identified in our catalogs). The nominal family-identification method, described in the Appendix, uses a very conservative search zone (followed by a control on the past convergence of the orbits). In order to demonstrate the margin we allow, we present a more in-depth test in the case of the Adelaide family here.

We use four nested boxes around the asteroid (525) Adelaide in osculating orbital elements (data from MPC catalog as of May 15, 2023), with the following parameters:

- Box 1 defined by the following differences in semimajor axis a, eccentricity e, inclination I, longitude of node Ω, and argument of perihelion ω: $(\delta a, \delta e, \delta I, \delta\Omega, \delta\omega) = (\pm 0.01, \pm 0.01, \pm 0.1°, 10°, 10°)$;
- Box 2 defined by the following differences in semimajor axis a, eccentricity e, inclination I, longitude of node Ω, and argument of perihelion ω: $(\delta a, \delta e, \delta I, \delta\Omega, \delta\omega) = (\pm 0.02, \pm 0.02, \pm 0.15°, 20°, 20°)$;
- Box 3 defined by the following differences in semimajor axis a, eccentricity e, inclination I, longitude of node Ω, and argument of perihelion ω: $(\delta a, \delta e, \delta I, \delta\Omega, \delta\omega) = (\pm 0.03, \pm 0.03, \pm 0.2°, 30°, 30°)$;
- Box 4 defined by the following differences in semimajor axis a, eccentricity e, inclination I, longitude of node

Ω, and argument of perihelion ω: $(\delta a, \delta e, \delta I, \delta\Omega, \delta\omega) = (\pm 0.035, \pm 0.035, \pm 0.25°, 35°, 35°)$.

Our nominal procedure described in the Appendix uses Box 3, where we identified all 79 Adelaide family members listed in Table A.2. Here are the data of asteroid populations found in the subsequent boxes: (i) Box 1 contains 74 asteroids, all Adelaide family members and no background objects, (ii) Box 2 contains 84 asteroids, all 79 Adelaide family members and 5 background objects, (iii) Box 3 contains 105 asteroids, all 79 Adelaide family members and 26 background objects, and (iv) Box 4 contains 135 asteroids, all 79 Adelaide family members and 56 background objects. The identified members of the Adelaide family reside in the interior two boxes (for most part already in Box 1). The background population of asteroids slowly ramps from the Box 2 stage[9]. These statistics make us believe that we are not missing any distant (and small) Adelaide members. A similar situation applies to other families as well.

Collisional comminution of family members beyond H_{break}? The bias-corrected population of the family members, as follows from our analysis, tells us about the current population several hundreds of thousands of years after the origin of the clusters. This population may have experienced some degree of collisional evolution over that interval, enough to disrupt some family members. As a result, we must verify whether the transition to a shallower magnitude distribution beyond $H_{\rm break}$ in the case of the Datura, Adelaide and Rampo families is not simply produced by collisional comminution.

We note that the size distribution of the main belt becomes shallow below 1 km in diameter, and its equivalent steepness at ≃500 m may be as small as $\gamma \simeq 0.3$ (see Fig. 1 in Bottke et al. 2020). Any submerged population introduced into this vast population of projectiles, such as a volume-limited new family, tends to equilibrate with the background (assuming disruption laws are the same for the background and family objects). The crucial issue with young asteroid families is the timescale of this process: has enough time passed since the origin of the family to reach equilibrium for members that are hundreds of meters?

In order to explore this issue we performed the following numerical experiment. We used the well-tested Monte Carlo code `Boulder` (e.g., Morbidelli et al. 2009; Vernazza et al. 2018) to track the collisional evolution of multiple small-body populations. Here we simulated both the internal impact/cratering/disruption processes within each of the populations and also the mutual collisional interaction of the populations (i.e., objects in one population may serve as impactors for the other and vice versa). The code version we adopted models the size-frequency distribution for each of the populations but does not include the orbital dynamics of the population members.

We used two populations: (i) the background population of main belt asteroids taken from Bottke et al. (2015a), and (ii) the young family population. We were only interested in a brief interval of time lasting ≤ 1 Myr (i.e., equal to the estimated age for the corresponding family).The origin of the simulation was the formation epoch of the family. The main belt population is effectively in equilibrium for the relevant sizes of about ten meters and larger, but the family population is expected to evolve with time; proving or disproving changes of the family size distribution at hundred meter and larger sizes was the goal of our simple test.

The initial size distribution of the family was equal to the best-fitting, bias-corrected solution from Sect. 4 with the following modification: we disregarded the breakpoint at $H_{\rm break}$ in the $\mathcal{M}2$ (and higher) class of solutions and continued the distribution with the power-exponent γ_1 from the first magnitude interval $(H_1, H_{\rm break})$. We considered 0.24 geometric albedo to convert absolute magnitude in Sect. 4 to sizes. Finally, we needed to specify parameters of the collisional interaction – intrinsic collisional probability p_i and mean relative velocity $\bar{v}$ at impact – within each of the populations and across them. This was done as follows.

The intrinsic values of p_i and $\bar{v}$ of the main belt population have been evaluated in many previous studies, and there is some small variation among them (related mostly to the smallest-size bodies used for their determination). We used $p_i = 2.9 \times 10^{-18}$ km^{-2} yr^{-1} and $\bar{v} = 5.3$ km s^{-1} (see Sect. 2.1 in Bottke et al. 2015a). For simplicity, the same values were taken for main belt projectiles impacting the young asteroid family population. The latter was deemed to be negligible in the relevant sizes of ten meters and larger (see Fig. 27), which allowed us to neglect family members as a meaningful population of impactors for main belt asteroids.

The tricky part of the calculation was to determine the intrinsic collisional parameters for the family population. This is because p_i and $\bar{v}$ depend on the orbital architecture of the family population, which experienced strong evolution immediately after the family formation event. The initially extremely compact cloud of fragments should first disperse in orbital mean anomaly (over a characteristic timescale of few thousands of years), and subsequently continues to disperse in longitude of node and perihelion (reaching about 20° interval for a ≃500 kyr old Datura family, e.g., Fig. 1). This highly dynamical situation implies that the intrinsic family values of p_i and $\bar{v}$ are also strongly time dependent. Importantly, because of the initial orbital similarity, the collision probabilities may also be very high.

Since assumptions of the most commonly used scheme to evaluate p_i and $\bar{v}$, notably the Öpik-Wetherill approach are not satisfied (see Öpik 1951; Wetherill 1967; Greenberg 1982), we used a more direct approach based on a numerical orbital integration of a finite sample of n bodies in the population (for details of the approach see, e.g., Marzari et al. 1996; Dahlgren 1998). Monitoring the orbits over a time interval ΔT, we recorded all mutual close encounters at a small-enough distance R (in our simulations we used R up to 0.002 au). The available number of pair combinations is $n_{\rm pair} = n(n-1)/2$. If N such encounters are found, we have an estimate

$$p_i \simeq \frac{N}{n_{\rm pair} R^2 \Delta T}. \tag{3}$$

Ideally, one should evaluate the whole congruence of encounters by varying the threshold distance R and verify that $N(R) \propto R^2$, such that p_i converges to a constant value. We verified this behavior is satisfied in our experiment. More importantly, as the orbits in the family undergo their dynamical evolution, we find that p_i changes as a function of time.

We considered the case of the Datura family as an exemplary case for our method. In order to track the characteristic orbital evolution of Datura members, we created a synthetic Datura family consisting of its 57 largest members (Table A.1). The initial configuration was created by propagating Datura's orbit backward in time until the argument of perihelion was $\omega \simeq 0°$ and true anomaly $f \simeq 150°$. We assumed an isotropic

[9] Taken very naively, namely just multiplying dimensions of the box in all searched orbital elements, the "volume" of the Box 4 is ≃2.3 larger than that of the Box 3. The number of background asteroids increased by a factor of 56/26 ≃ 2.15. This may indicate roughly uniform, but very sparse, population of background population at the location of the Adelaide family.

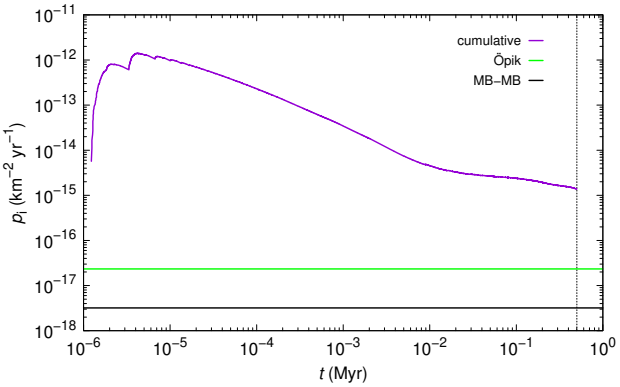

Fig. 26. Intrinsic collisional probability $\bar{p}_i$ of Datura members with respect to each other based on data from numerical integration of $n = 57$ asteroids of a synthetic family and using Eq. (3). Time since origin of the family at the abscissa also represents the ΔT timescale in the denominator of Eq. (3). The initially extremely compact configuration of Datura fragments results in very large $\bar{p}_i$ values during the first few revolutions about the Sun. This is followed by a decline reflecting asteroid dispersal which has two phases: (i) first along the elliptic orbit, completed in ≃(2–3) kyr (corresponding to change in slope of $\bar{p}_i(t)$ power-law approximation), (ii) followed with a phase during which the secular angles (longitude of node and perihelion) drift from each other. This latter phase has not been completed yet for very young families (Fig. 1). For this reason the terminal $\bar{p}_i$ value is nearly two orders of magnitude larger than the formal collision probability computed with the Öpik-Wetherill approach (orange line), in which only the values of (a, e, I) would be taken into consideration and the secular angles (Ω, ω) considered uniformly distributed in the whole interval $(0°, 360°)$. The reference mean value of the intrinsic collisional probability for the main belt population, $p_i \simeq 3 \times 10^{-18}$ km^{-2} yr^{-1}, is shown by the gray horizontal line for reference.

and size-dependent velocity ejection field

$$V(D) = 1\,\mathrm{m\,s^{-1}} \left(\frac{D}{2\,\mathrm{km}} \right)^{-0.5} , \tag{4}$$

which allows us to create a configuration that, in the (a, e) and (a, i) planes, resembles the distribution of Datura members (e.g., Nesvorný & Vokrouhlický 2006; Vokrouhlický et al. 2017a; for instance semimajor axes spread ±0.001 au). We used symplectic integrator `rmvs3`, part of a well-tested package `swift`[10], and included perturbations from eight planets and the massive dwarf planets Ceres and Vesta. We also randomly assigned thermal accelerations (i.e., the Yarkovsky effect) to the family members in the transverse direction. The smallest members in our simulation were thus given semimajor axis drift rates up to $\mathrm{d}a/\mathrm{d}t \simeq \pm 0.0006$ au Myr^{-1}. We determined mutual distances of all simulated particles at every timestep of 3.6525 days, seeking very close encounters for determination of p_i from Eq. (3) (determination of the encounter configurations was implemented on-line by seeking minima on the memory-sorted mutual distances), and propagated the synthetic family for a timespan of 500 kyr corresponding to the Datura age (e.g., Nesvorný et al. 2006; Vokrouhlický et al. 2009, 2017a).

We evaluated a "cumulative" $\bar{p}_i$ value by taking ΔT in Eq. (3) the current epoch in the integrated system and counting N from all encounters until that moment. The results are shown in Fig. 26. We find that $\bar{p}_i$ peaks at ≃10 yr, representing three revolutions about the Sun. At that time the fragment configurations stay orbitally compact but encounters are beginning to decrease as the orbital angles begin to spread. The peak

[10] http://www.boulder.swri.edu/~hal/swift.html

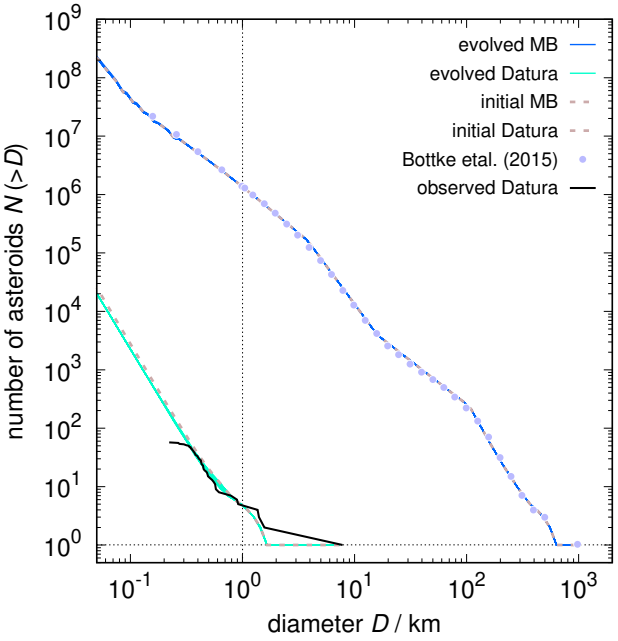

Fig. 27. Initial and final size distribution of the asteroid main belt (blue) and the synthetic Datura family (cyan) from the 500 kyr lasting simulation of the `Boulder` code. Intrinsic collisonal probabilities and impact velocities as described in the text. The observed Datura family population from Table A.1 shown by the black curve. No evolution is seen in both populations over the tested timescale and for the sizes displayed.

value $\bar{p}_i \simeq 10^{-12}$ km^{-2} yr^{-1} is six orders of magnitude larger than the mean value over the main belt population. This value obviously rapidly decreases in time, but at 500 kyr, which is the current epoch for Datura family, it still attains $\bar{p}_i \simeq 1.38 \times 10^{-15}$ km^{-2} yr^{-1}, namely three orders of magnitude larger than the mean value for the main belt. At face value, using this value alone, one would think that post family-formation collisions cannot and should not be neglected.

However, the mean encounter velocities over the age of the Datura family are very small; we find $\bar{v} \simeq 36$ m s^{-1}, with the full range of 0.3 to 500 m s^{-1}. As much as these values are impressive[11], one may anticipate whether internal or external (main belt) impactors would be more important for the Datura-family collisional evolution. The intrinsic collisional probability of Datura members between each other is about three orders of magnitude larger than the probability being hit by background main belt projectiles. However, the main belt impactor population is about four orders of magnitude more numerous (Fig. 27). Therefore, we expect that main belt projectiles will dominate collisional evolution in the family.

Finally, it is useful to mention that catastrophic breakups are characterized by the critical impact specific energy $Q^\star_\mathrm{D}$, namely the energy per unit target mass delivered by the projectile required for catastrophic disruption of the target (i.e., such that one-half the mass of the target body escapes). Many studies have dealt with this important quantity (see Bottke et al. 2015a, for review), but here we assume a simple relation (density ρ also in cgs units)

$$Q^\star_\mathrm{D} = 9.0 \times 10^7\,\mathrm{erg\,g^{-1}} \left(\frac{D}{2\,\mathrm{cm}} \right)^{-0.53} + 0.5\,\mathrm{erg\,cm^{-3}} \rho \left(\frac{D}{2\,\mathrm{cm}} \right)^{1.36} , \tag{5}$$

[11] We found it interesting to present some details of this numerical experiment, since we are not aware of a similar work previously published. It might be used as a template for studies of other very young families in the future.

whose constants have been adjusted provide a global stationary solution for the main belt asteroids (see also Bottke et al. 2020, for context). The critical size of a projectile able to catastrophically disrupt a target of size D scales as $\propto (Q_{\rm D}^{\star}/\bar{v}^2)^{1/3}\, D$ and this minimizes the role of internal collisions in young families because impact velocities $\bar{v}$ are low.

We ran the `Boulder` code for a 500 kyr timespan and obtained results shown in Fig. 27. No change in the family size distribution for $D > 50$ m was recorded, likely because the evolution timespan was too short. In families, the change in their size frequency distribution propagates from small to larger sizes, and in 500 kyr it only reaches the ≃10 cm range within the Datura family. Similar results were obtained for Adelaide and Rampo families too.

Summing up the previous simulations, we conclude that collisional evolution over the timescales corresponding to the ages of the very young families is not capable of producing a transition to a shallower segment of the family size distribution at about 300–400 m. If true, the bias-corrected family population from the current-date observations correspond also to the population of members created at the family origin.

Further results and future outlooks. The estimated parameters of the magnitude distributions obtained above may serve for additional consistency checks. For instance, assuming the bias-corrected populations are representative of those generated right after disruption of the parent body of the family at the observed sizes, we may use the estimated mass in small members to determine further quantities. In the case of the Adelaide family we found $m_{\rm frag}/m_{\rm LF} \simeq 0.0085$. With that number, we may estimate (the minimum) size of the crater on (525) Adelaide that has been formed. If we take crater depth to be ≃1/10–1/5 of its radius (e.g., Melosh 1989), and $D_{525} \simeq 9.4$ km the size of (525) Adelaide, a simple calculation shows that a crater with $D_{\rm crat} \simeq 3.6$–3.9 km would have about the same volume fraction in (525) Adelaide. This is still a reasonable number. Additionally, assuming crater to projectile size ratio of ≃10–20 (e.g., Bottke et al. 2020), we may estimate the projectile size to about $d_{\rm proj} \simeq 180$–390 m. The number of 10 km size asteroids in the inner main belt is $N_{10} \simeq 300$ (e.g., Masiero et al. 2011), and the number of 180–390 m objects in the main belt $N_{\rm proj} \simeq (1$–$5) \times 10^7$ (e.g., Bottke et al. 2020). Considering the mean intrinsic collision probability in the main belt $p_{\rm i} \simeq 2.8 \times 10^{-18}$ km^{-2} yr^{-1}, we may estimate the frequency of 180–390 m projectiles impacting a 10 km inner main belt target to about $f \simeq p_{\rm i} R^2 N_{\rm proj} N_{10} \simeq (0.2$–$1) \times 10^{-6}$ yr^{-1}. This results in a characteristic timescale of ≃1–5 Myr, which is well comparable with the estimated age of the Adelaide family (about 540 kyr, e.g., Vokrouhlický et al. 2021b). While highly simplified, this reasoning points to rough consistency between the Adelaide family origin and the produced fragment population.

Very young asteroid families will certainly occupy interest of planetary scientists in the forthcoming decade. While theoretical studies will continue, perhaps even more important input is expected on the observational side. The planned powerful surveys, such as the *Vera C. Rubin* observatory (e.g., Schwamb et al. 2023), promise to increase the known inventory of these clusters by an order of magnitude, pushing the completeness near to the absolute magnitude 20 (at least for clusters in the inner main belt). Unlike the case of large and old asteroid families, the identification of the very young families may be still a straightforward task (profiting from the 5D arena of the osculating orbital elements and a possibility to recognize interlopers using backward orbital propagation). The magnitude distribution of a complete population of members may be set much more reliably, including the critical interval of H in between 19 and 20 magnitude.

Acknowledgements. We thank the referee for very useful suggestions on the submitted version of the paper. We are grateful to the Catalina Sky Survey staff, Eric Christensen and Franck Shelly in particular, for providing us the CSS observations in between 2013 and 2022 in a user-friendly format and allowing us to use them for this research. This work was supported by the Czech Science Foundation (grant 21-11058S).

References

Asphaug, E., Collins, G., & Jutzi, M. 2015, in Asteroids IV, eds. P. Michel, F. E. DeMeo, & W. F. Bottke, 661
Bottke, W. F., Brož, M., O'Brien, D. P., et al. 2015a, in Asteroids IV, eds. P. Michel, F. E. DeMeo, & W. F. Bottke, 701
Bottke, W. F., Vokrouhlický, D., Walsh, K. J., et al. 2015b, Icarus, 247, 191
Bottke, W. F., Vokrouhlický, D., Ballouz, R. L., et al. 2020, AJ, 160, 14
Carruba, V., Ramos, L. G. M., & Spoto, F. 2020, MNRAS, 493, 2556
Christensen, E., Africano, B., Farneth, G., et al. 2019, in EPSC-DPS Joint Meeting 2019, EPSC-DPS2019-1912
Dahlgren, M. 1998, A&A, 336, 1056
Durda, D. D., Bottke, W. F., Nesvorný, D., et al. 2007, Icarus, 186, 498
Greenberg, R. 1982, AJ, 87, 184
Hirayama, K. 1918, AJ, 31, 185
Jacobson, S. A., & Scheeres, D. J. 2011, Icarus, 214, 161
Jutzi, M., Holsapple, K., Wünneman, K., & Michel, P. 2015, in Asteroids IV, eds. P. Michel, F. E. DeMeo, & W. F. Bottke, 679
Marzari, F., Scholl, H., & Farinella, P. 1996, Icarus, 119, 192
Masiero, J. R., Mainzer, A. K., Grav, T., et al. 2011, ApJ, 741, 68
Masiero, J. R., DeMeo, F. E., Kasuga, T., & Parker, A. H. 2015, in Asteroids IV, eds. P. Michel, F. E. DeMeo, & W. F. Bottke, 323
Melosh, H. J. 1989, Impact Cratering: A Geologic Process (Oxford: Oxford University Press)
Michel, P., Richardson, D. C., Durda, D. D., Jutzi, M., & Asphaug, E. 2015, in Asteroids IV, eds. P. Michel, F. E. DeMeo, & W. F. Bottke, 341
Migliorini, F., Zappalà, V., Vio, R., & Cellino, A. 1995, Icarus, 118, 271
Morbidelli, A., Bottke, W. F., Nesvorný, D., & Levison, H. F. 2009, Icarus, 204, 558
Mothé-Diniz, T., & Nesvorný, D. 2008, A&A, 486, L9
Nesvorný, D., & Vokrouhlický, D. 2006, AJ, 132, 1950
Nesvorný, D., Vokrouhlický, D., & Bottke, W. F. 2006, Science, 312, 1490
Nesvorný, D., Brož, M., & Carruba, V. 2015, in Asteroids IV, eds. P. Michel, F. E. DeMeo, & W. F. Bottke, 297
Nesvorný, D., Vokrouhlický, D., Shelly, F., et al. 2023, Icarus, submitted
Novaković, B., & Radović, V. 2019, RNAAS, 3, 105
Novaković, B., Vokrouhlický, D., Spoto, F., & Nesvorný, D. 2022, Celest. Mech. Dyn. Astron., 134, 34
Öpik, E. J. 1951, Proc. R. Irish Acad. Sect. A, 54, 165
Polishook, D., Moskovitz, N., Binzel, R. P., et al. 2014, Icarus, 233, 9
Pravec, P., & Vokrouhlický, D. 2009, Icarus, 204, 580
Pravec, P., Vokrouhlický, D., Polishook, D., et al. 2010, Nature, 466, 1085
Pravec, P., Fatka, P., Vokrouhlický, D., et al. 2018, Icarus, 304, 110
Pravec, P., Fatka, P., Vokrouhlický, D., et al. 2019, Icarus, 333, 429
Press, W. H., Teukolsky, S. A., Vetterling, W. T., & Flannery, B. P. 2007, Numerical Recipes: The Art of Scientific Computing (Cambridge: Cambridge University Press)
Rosaev, A., & Plávalová, E. 2016, ArXiv e-prints [arXiv:1612.04951]
Rosaev, A., & Plávalová, E. 2017, Planet. Space Sci., 140, 21
Rosaev, A., & Plávalová, E. 2018, Icarus, 304, 135
Schwamb, M. E., Jones, R. L., Yoachim, P., et al. 2023, ApJS, 266, 22
Spoto, F., Milani, A., & Knežević, Z. 2015, Icarus, 257, 275
Tricarico, P. 2017, Icarus, 284, 416
Vernazza, P., Binzel, R. P., Rossi, A., Fulchignoni, M., & Birlan, M. 2009, Nature, 458, 993
Vernazza, P., Brož, M., Drouard, A., et al. 2018, A&A, 618, A154
Vokrouhlický, D. & Nesvorný, D. 2008, AJ, 136, 280
Vokrouhlický, D., Brož, M., Bottke, W. F., Nesvorný, D., & Morbidelli, A. 2006, Icarus, 182, 118
Vokrouhlický, D., Nesvorný, D., & Bottke, W. F. 2008, ApJ, 672, 696
Vokrouhlický, D., Ďurech, J., Michałowski, T., et al. 2009, A&A, 507, 495
Vokrouhlický, D., Ďurech, J., Polishook, D., et al. 2011, AJ, 142, 159
Vokrouhlický, D., Pravec, P., Ďurech, J., et al. 2017a, A&A, 598, A91
Vokrouhlický, D., Pravec, P., Ďurech, J., et al. 2017b, AJ, 153, 270
Vokrouhlický, D., Brož, M., Novaković, B., & Nesvorný, D. 2021a, A&A, 654, A75
Vokrouhlický, D., Novaković, B., & Nesvorný, D. 2021b, A&A, 649, A115
Wetherill, G. W. 1967, J. Geophys. Res., 72, 2429

Appendix A: Members of the very young families

Here we provide an information about membership in the very young asteroid families studied in this paper. Our approach to obtain these results is based on two criteria. First, we search for asteroids located in the vicinity of the largest member in the 5D space of osculating orbital elements (disregarding longitude in orbit λ): semimajor axis a, eccentricity e, inclination I, longitude of node Ω, and argument of perihelion ω. Unlike in Nesvorný & Vokrouhlický (2006), we do not use any specific metric function, but simply select all asteroids with orbits in a certain box. In particular, we let the orbital elements vary by the following limits: (i) semimajor axis by ±0.03 au, (ii) eccentricity by ±0.03, (iii) inclination by ±0.2°, and (iv) longitude of node and argument of perihelion both by ±30°. These values are larger than the short-period oscillations of these elements due to planetary perturbations, and conservative enough to sense the population even to the smallest currently detectable sizes (note that small members might have been ejected with larger velocity than the larger ones, constituting the family core). Given the large increase in number of discovered asteroids, there is a small but nonzero chance that such a simple selection method may associate background (unrelated) objects to the family even in the vast 5D space. For that reason, we perform in the second step a convergence control. We numerically integrate orbits of all identified asteroids backward in time for 2 Myr. To keep things simple, we use only nominal (best-fit) initial data at MJD epoch 60,000.0 and include only gravitational perturbations from all planets (disregarding thermal accelerations).[12] The planetary configuration at the initial epoch is obtained from the JPL ephemerides file DE 421. As a result, the purpose of this simulation is not to accurately determine the age of the family, which is for most cases known from previous studies, but to eliminate possible interloping objects. We found that the secular angles in the interloper cases show a rapid divergence from the largest body in the family and may be easily identified. Obviously, we eliminated these objects from our analysis of the size distribution of the family members. There was only a limited amount of such objects found. The most crowded situation occurred for Datura family, where we eliminated 80 such objects, i.e., little less than the family members (who are strongly clustered in the simple 5D box of orbital elements that we considered for family-member search).

[12] We use a well-tested and publicly available integration package `swift` (`http://www.boulder.swri.edu/~hal/swift.html`) with a short timestep of 2 d. We output the asteroid heliocentric state vectors every 5 yr and monitor convergence of the secular angles Ω and ϖ toward the reference values of the largest member in the family.

Table A.1. Datura family as of June 2023.

Asteroid		H (mag)	a (au)	e	I (deg)	Ω (deg)	ω (deg)	CSS
1270	Datura	12.54	2.2344232	0.2080399	5.98629	97.77551	259.06896	Y
60151	1999 UZ6	16.35	2.2347805	0.2078266	5.99466	96.68391	260.77419	Y
89309	2001 VN36	16.48	2.2356444	0.2064328	6.01966	92.81960	267.16899	Y
90265	2003 CL5	16.08	2.2347649	0.2074858	5.99650	95.55568	262.11246	Y
203370	2001 WY35	17.33	2.2352682	0.2074548	5.98927	96.71788	260.76103	Y
215619	2003 SQ168	17.24	2.2343739	0.2080248	5.98761	97.36200	259.62134	Y
338309	2002 VR17	17.68	2.2345469	0.2077371	5.99159	96.68295	260.80932	Y
429988	2013 PZ36	17.95	2.2306873	0.2109170	5.82996	102.85349	248.77348	Y
433382	2013 ST71	18.09	2.2343697	0.2079372	5.98521	97.92635	259.05669	Y
452713	2005 YP136	18.46	2.2367817	0.2052885	6.04942	86.12897	276.54525	Y
485010	2009 VS116	18.23	2.2361205	0.2051146	6.06774	85.69555	277.53365	Y
553350	2011 KT10	18.15	2.2361705	0.2068784	6.02362	92.38721	267.95500	Y
585600	2018 VR79	18.54	2.2350642	0.2074864	5.98893	97.32214	259.95573	Y
	2002 RH291	17.97	2.2349777	0.2076290	5.99691	95.64466	262.24539	Y
	2002 UU58	19.97	2.2347195	0.2074394	5.99799	96.59631	261.33505	
	2003 UD112	18.10	2.2347778	0.2073396	5.99912	95.41269	263.14733	Y
	2005 RK54	18.75	2.2348344	0.2066777	6.03197	92.65329	267.58009	
	2006 KA77	18.31	2.2343902	0.2083194	5.98156	99.49835	256.42782	Y
	2006 SY376	20.30	2.2329680	0.2096354	5.96933	107.19877	245.09390	
	2006 SD382	18.91	2.2361239	0.2055712	6.05939	85.86581	277.02849	Y
	2006 WV222	18.80	2.2350979	0.2080650	5.98696	97.78267	259.39354	Y
	2007 RM332	18.47	2.2351994	0.2077589	5.98292	98.46057	258.26665	Y
	2008 YV51	18.60	2.2353599	0.2075360	5.98733	97.48832	259.71301	Y
	2010 VN260	19.20	2.2349143	0.2073926	5.99770	96.14005	262.02148	Y
	2010 VU261	19.10	2.2346754	0.2076944	5.99159	96.65770	260.93281	Y
	2010 VB265	19.10	2.2348391	0.2075374	5.99878	96.29429	261.51547	Y
	2012 VN143	19.32	2.2346189	0.2074989	5.99550	96.99693	260.66846	
	2014 NZ88	18.80	2.2353179	0.2072581	5.98828	96.96231	260.64555	Y
	2014 OY85	19.50	2.2343694	0.2085063	5.97725	100.94642	253.92579	
	2014 OA86	18.87	2.2349119	0.2078508	5.97656	100.39381	255.53971	Y
	2014 OE206	19.26	2.2354740	0.2070515	5.99678	96.10416	262.05661	Y
	2014 OR378	18.77	2.2352076	0.2075890	5.98585	97.77828	259.17541	Y
	2014 WL96	19.30	2.2368677	0.2067078	6.00707	93.95385	265.59361	
	2014 WT96	18.93	2.2355619	0.2072284	5.99606	95.93259	262.19506	
	2015 DY94	18.20	2.2346085	0.2075363	5.99356	96.48915	261.34069	Y
	2015 PD191	20.00	2.2360619	0.2070593	6.02521	93.22656	266.76523	
	2015 PQ47	19.17	2.2343287	0.2077176	5.99164	97.27727	259.91321	
	2015 PH144	19.56	2.2337492	0.2084264	5.98369	98.81562	257.09515	
	2015 PR301	18.87	2.2343558	0.2078212	5.98601	98.26718	258.53367	
	2015 QW31	19.00	2.2342126	0.2078737	5.98459	98.21808	258.43923	
	2015 SS31	18.84	2.2351942	0.2063313	6.00527	91.16595	268.71019	Y
	2015 TL455	18.59	2.2345918	0.2076533	5.99230	97.58170	259.65709	Y
	2015 WQ25	18.70	2.2347622	0.2074942	5.99209	96.92848	260.47264	Y
	2015 XK88	18.63	2.2341292	0.2082101	5.98363	99.13007	256.75539	Y
	2015 XX321	19.13	2.2349203	0.2073029	5.99831	96.45517	261.40030	Y
	2015 XQ432	18.80	2.2347230	0.2073054	5.99311	96.44434	261.32662	Y

Notes. Osculating heliocentric orbital elements at epoch MJD 60,000.0 from the MPC catalog: semimajor axis a, eccentricity e, inclination I, longitude of node Ω, and argument of perihelion ω. singleopposition orbits are listed at the end of the table. The third column gives the absolute magnitude H. The last column indicates, whether the asteroid has been detected by CSS during the phase 2 operations (Y=yes). We note two very small, singleopposition asteroids 2016 PL51 and 2022 RB57, very likely members of the Datura family too. However, their orbits, based on observations spanning short arcs (less than a week in the case of 2016 PL51), are still very uncertain. We include (429988) 2013 PZ36 residing on a rather chaotic orbit (most likely interacting with the exterior E3/10 mean motion resonance with the Earth), such that proving its membership to the Datura family would require an extensive work beyond the scope of this paper (see also Fig. 1). Luckily, the results discussed in Sect. 4 are not overly sensitive to the decision about Datura membership of this body.

Table A.1. continued.

Asteroid	H (mag)	a (au)	e	I (deg)	Ω (deg)	ω (deg)	CSS
2015 XK452	18.98	2.2348068	0.2074621	5.99415	97.07086	260.30732	Y
2016 TW15	18.70	2.2346167	0.2077361	5.99193	97.14749	260.35782	Y
2016 TR115	18.70	2.2348542	0.2078892	5.98988	97.68880	259.59729	Y
2017 QX88	18.88	2.2370037	0.2053516	6.06398	85.78189	277.15110	Y
2017 SU3	18.91	2.2352968	0.2074508	5.98488	97.47714	259.99874	Y
2017 SV143	18.80	2.2354487	0.2049571	6.06182	86.32039	276.61565	Y
2017 UW137	19.75	2.2343672	0.2084085	5.97502	101.13381	254.12998	Y
2017 UU155	19.62	2.2365893	0.2069006	6.00884	93.82864	265.81621	Y
2017 VP37	19.40	2.2352166	0.2075381	5.99312	97.08958	260.46478	Y
2017 WC50	19.53	2.2352780	0.2073674	5.99337	96.33838	261.68738	
2018 TM7	18.71	2.2347907	0.2075211	5.98873	97.80903	259.29224	Y
2018 UN34	19.25	2.2352820	0.2068990	5.99899	96.01196	262.59590	Y
2018 UL40	19.10	2.2353244	0.2069677	6.00250	96.17580	262.28729	Y
2019 QA14	18.60	2.2351143	0.2078881	5.99236	97.28433	260.08707	Y
2019 SE28	19.16	2.2342820	0.2087329	5.98412	99.30327	256.39995	Y
2019 XJ15	19.12	2.2350562	0.2073834	6.00613	95.41326	263.12590	Y
2020 OS89	19.54	2.2348379	0.2075650	6.00508	93.45550	264.93955	
2020 PM28	19.24	2.2352071	0.2077160	5.99066	97.81753	259.47920	Y
2021 RB114	18.60	2.2352733	0.2073676	5.99044	96.69883	260.81727	Y
2022 QC148	19.50	2.2343589	0.2078442	5.99308	97.08424	260.07491	
2022 SV168	19.59	2.2348466	0.2051558	6.06436	86.74092	275.74315	
– Singleopposition members –							
2014 WG250	18.95	2.2352239	0.2075190	5.98785	97.36655	259.84769	
2014 WM249	19.19	2.2339095	0.2075368	5.98235	97.79023	259.01686	
2015 TU306	19.60	2.2349386	0.2067806	6.01564	95.68816	263.34206	
2016 PY22	19.44	2.2360027	0.2069173	6.02658	92.76382	267.85893	
2017 OS162	19.49	2.2360582	0.2070355	5.98009	90.91999	267.41699	
2017 OU162	19.69	2.2353099	0.2074271	5.98822	97.34285	260.05416	
2017 SG152	19.00	2.2357888	0.2064416	6.01963	93.43504	266.60818	Y
2017 SV193	19.60	2.2352198	0.2074399	5.99136	96.97981	260.72387	Y
2017 SC233	19.20	2.2350514	0.2074005	6.00705	93.16523	265.47990	
2017 SS269	19.90	2.2360231	0.2070277	6.00573	95.79973	263.47065	
2019 TD28	19.60	2.2368243	0.2075650	6.01491	94.64557	265.09847	Y
2020 QM36	19.00	2.2349968	0.2076282	5.98836	97.10501	260.48247	Y
2020 RR103	19.80	2.2361572	0.2077930	5.98241	90.88493	267.16232	Y
2020 UV37	19.30	2.2354422	0.2074241	5.97418	90.97581	267.30544	Y
2021 NF47	19.49	2.2350049	0.2075666	5.98830	97.42570	259.67732	Y
2021 NK57	19.14	2.2353946	0.2069712	5.99919	95.52787	262.99252	Y
2021 PX107	19.22	2.2352389	0.2073418	5.98930	97.13408	260.30247	Y
2021 QZ40	19.75	2.2350184	0.2074293	5.99078	96.79357	260.66997	
2021 RE149	19.00	2.2349079	0.2077411	5.98546	98.19857	258.44555	Y
2021 VU20	20.32	2.2355854	0.2063734	6.00005	95.48181	263.86595	
2022 PN15	19.82	2.2352065	0.2070323	6.02051	94.91401	264.61153	
2022 QK69	19.85	2.2361785	0.2073031	5.99880	95.16386	263.81182	
2022 QT171	19.62	2.2363260	0.2071205	6.02165	94.40238	265.28039	
2022 SO76	19.43	2.2339303	0.2084255	5.98316	98.95475	256.96663	
2022 TV22	20.14	2.2362992	0.2055041	6.06042	85.66342	276.96670	

Table A.2. Adelaide family as of June 2023.

Asteroid		H (mag)	a (au)	e	I (deg)	Ω (deg)	ω (deg)	CSS
525	Adelaide	12.17	2.2459455	0.1020388	5.99835	203.35936	263.96182	Y
422494	2014 SV342	18.37	2.2457873	0.1036634	6.01316	201.90211	262.11221	Y
452322	2000 GG121	18.43	2.2459962	0.0990051	6.05840	197.12857	277.42396	Y
463394	2013 GV28	18.56	2.2452544	0.1014759	6.00185	203.34261	265.44077	Y
475474	2006 SZ152	18.58	2.2446196	0.1025679	5.98782	204.84491	263.14855	Y
486081	2012 UX41	18.54	2.2458709	0.1018798	6.01195	200.73242	265.92554	Y
504375	2007 VV73	18.76	2.2455021	0.1034966	6.01373	200.64920	264.76138	Y
517580	2014 UZ170	18.68	2.2457137	0.1015922	6.00769	200.32247	269.68162	Y
534611	2014 UC204	18.18	2.2458760	0.1010302	6.02623	199.84308	272.15198	Y
545614	2011 SA45	18.41	2.2457694	0.1022064	6.00750	201.81455	264.31208	Y
552867	2010 UF125	18.78	2.2449504	0.1025609	6.01004	202.13835	266.85951	Y
555571	2014 AD31	18.51	2.2457958	0.1009470	6.02260	200.55360	270.49477	Y
569552	2005 UK370	19.01	2.2455102	0.1014688	6.02424	200.81248	268.01004	Y
572830	2008 US17	18.57	2.2455380	0.1000395	6.04296	198.32560	273.73347	Y
572868	2008 UR182	18.40	2.2458141	0.1034843	6.02337	200.30854	263.50713	Y
578969	2014 JA2	18.26	2.2457211	0.1010352	6.03014	199.49735	269.87273	Y
593790	2015 XZ90	18.70	2.2449726	0.1014565	5.99848	203.78817	264.25467	Y
616487	2005 VP83	18.45	2.2456512	0.1016943	6.02430	200.22763	267.30317	Y
	2004 HU76	19.02	2.2462293	0.1005166	6.00980	202.63100	267.20087	Y
	2004 HJ85	18.97	2.2461326	0.1032087	6.03593	200.54895	263.66537	Y
	2005 UF193	18.77	2.2454086	0.1038225	6.01911	200.93875	261.58535	Y
	2006 SK449	18.40	2.2456295	0.1013371	6.02272	200.42520	271.19772	Y
	2007 TA504	18.90	2.2455486	0.1024368	6.02680	200.28214	268.89512	Y
	2007 VT345	18.58	2.2449214	0.1035204	5.99871	203.77264	262.38520	Y
	2008 ET179	18.60	2.2450348	0.1025046	6.00338	202.63850	266.26648	Y
	2008 UR414	18.63	2.2460790	0.0989092	6.02968	201.69890	272.77329	Y
	2009 WJ157	18.77	2.2464285	0.1016017	6.01107	202.07146	265.29561	Y
	2010 VC228	18.33	2.2450406	0.1014959	6.03451	198.81306	273.39747	Y
	2010 VF260	18.60	2.2450148	0.1034408	6.04766	197.20466	270.60213	Y
	2010 XB115	18.81	2.2448215	0.1031887	6.00795	201.45005	265.44057	Y
	2012 TM342	19.30	2.2451705	0.1015429	6.00110	202.85893	265.02778	
	2013 CH251	19.43	2.2457832	0.1021203	6.00697	202.66417	264.04047	Y
	2013 GR162	18.80	2.2457624	0.1026941	6.00444	202.30810	263.28291	Y
	2013 HB97	19.80	2.2463044	0.1003166	6.02739	200.10111	272.11349	
	2013 TY219	18.96	2.2442386	0.1035677	5.99071	204.30989	262.02986	Y
	2013 TR236	19.54	2.2454223	0.1028989	6.01398	202.86209	264.25702	Y
	2014 EQ81	19.10	2.2469478	0.0999236	6.05462	197.32994	275.67967	Y
	2014 EU96	19.20	2.2464881	0.1040363	6.01320	200.66878	262.24741	Y
	2014 EM164	18.98	2.2459219	0.1031170	5.99009	204.47170	260.80897	Y
	2014 JY105	19.10	2.2459512	0.0987461	6.03208	201.11692	273.10746	Y
	2014 WM167	18.95	2.2458331	0.1018454	6.00962	202.17318	267.55573	Y
	2015 BE285	19.05	2.2449165	0.1039514	5.99999	203.11323	261.33797	Y
	2015 HU72	18.95	2.2452445	0.1031607	6.00944	202.19152	264.15943	Y
	2015 RM186	18.73	2.2460358	0.0984971	6.06417	196.43719	279.45108	Y
	2015 TD44	19.26	2.2444571	0.1025243	5.98632	204.98118	260.23068	Y
	2015 UR18	19.30	2.2454281	0.1021862	6.03178	200.65949	265.28313	Y
	2015 XC92	19.07	2.2460168	0.1009429	6.04263	200.06013	269.07119	
	2016 AH353	19.77	2.2460923	0.1013139	6.01534	202.02955	267.90961	
	2016 AL322	18.90	2.2456315	0.1026982	6.01532	202.92759	262.78436	Y
	2016 CP95	19.33	2.2463603	0.1003278	6.02127	200.61828	271.25649	
	2016 CX104	19.24	2.2448809	0.1035784	5.98559	205.29467	258.78148	Y

Notes. Osculating heliocentric orbital elements at epoch MJD 60,000.0 from the MPC catalog: semimajor axis a, eccentricity e, inclination I, longitude of node Ω, and argument of perihelion ω. singleopposition orbits are listed at the end of the table. The third column gives the absolute magnitude H. The last column indicates, whether the asteroid has been detected by CSS during the phase 2 operations (Y=yes). We note asteroid (159941) 2005 WV178 in the near vicinity of the Adelaide family, which we discard from the membership due to a dubious convergence to (525) Adelaide in the past Myr.

Table A.2. continued.

Asteroid	H (mag)	a (au)	e	I (deg)	Ω (deg)	ω (deg)	CSS
2016 EX318	19.50	2.2449848	0.1030240	5.98796	204.87999	260.79999	Y
2016 FR33	19.10	2.2458347	0.1015699	6.05834	196.65477	274.01002	Y
2016 FA34	18.86	2.2455945	0.1024636	6.01441	201.96964	265.06660	Y
2016 GO11	18.72	2.2450053	0.1037665	5.98548	205.07788	259.12530	Y
2016 QE71	18.40	2.2454966	0.1029550	6.01495	201.16100	266.00988	Y
2016 TN41	18.90	2.2446126	0.1043580	5.98344	205.11808	258.91716	
2016 UO110	19.06	2.2454466	0.1026978	5.99586	203.55032	263.93640	Y
2017 AU38	18.78	2.2458978	0.1013304	6.00496	202.56750	266.13825	Y
2017 HL72	19.28	2.2459566	0.0998460	6.02303	200.55185	271.45608	Y
2017 RS100	19.33	2.2449371	0.1039013	6.00073	204.79324	259.00262	Y
2017 TG26	18.87	2.2448290	0.1044112	5.98989	204.40015	259.95117	Y
2017 UF65	19.32	2.2446513	0.1035296	6.00813	202.33968	263.80059	Y
2017 WP50	19.10	2.2444171	0.1030306	6.00350	203.01479	264.40475	
2019 BT11	19.11	2.2453842	0.1009102	6.02325	200.50607	270.84753	Y
2019 TC62	19.20	2.2471638	0.0996640	6.05763	196.55998	277.07321	Y
2019 YE29	19.77	2.2457962	0.1006684	6.02946	200.43589	269.04712	Y
2019 YU35	19.86	2.2460175	0.1008068	6.02944	202.15923	266.45230	
2020 ML45	19.00	2.2459836	0.1010309	6.02237	201.82072	267.71323	
2020 PM79	19.50	2.2452151	0.1027546	6.00307	204.32861	262.16107	
2022 BM6	19.30	2.2454318	0.1021906	6.00621	202.54005	266.53136	Y
2022 CU16	18.98	2.2449320	0.1035621	6.01424	202.07267	263.45712	Y
2022 TC6	18.99	2.2453803	0.1013650	6.00377	203.09324	265.02593	
– Singleopposition members –							
2022 BM50	19.97	2.2451736	0.1020011	6.00018	201.42183	268.13980	Y
2023 AH4	20.32	2.2458161	0.1016177	6.00306	203.14933	265.55282	
2023 BX6	20.23	2.2454761	0.1028669	5.99652	203.75734	262.07433	
2023 BZ6	20.11	2.2461186	0.1005071	6.01469	201.61036	269.59264	
2023 BP9	20.53	2.2493354	0.1021673	6.02529	199.84371	272.57419	
2023 BS11	20.57	2.2470465	0.1005654	6.01926	200.54636	271.10920	

Table A.3. Hobson family as of June 2023.

Asteroid		H (mag)	a (au)	e	I (deg)	Ω (deg)	ω (deg)	CSS
18777	Hobson	15.12	2.5633566	0.1833929	4.32167	105.43986	180.62462	Y
57738	2001 UZ160	15.27	2.5643655	0.1804590	4.31695	104.86638	181.39287	Y
363118	2001 NH14	17.34	2.5640791	0.1802580	4.31088	105.05377	181.32416	Y
381414	2008 JK37	17.70	2.5644935	0.1801728	4.32092	104.22939	181.70561	Y
436620	2011 LF12	17.35	2.5623364	0.1840800	4.32629	104.88486	180.38868	Y
450571	2006 JH35	17.64	2.5622205	0.1830388	4.31799	105.19338	180.53430	Y
465404	2008 HQ46	17.67	2.5640097	0.1819144	4.31527	105.23235	182.39770	Y
520394	2014 JJ10	18.15	2.5636411	0.1819023	4.31680	105.02491	180.59212	Y
537249	2015 HM190	17.60	2.5618837	0.1853909	4.32936	105.06573	181.29952	Y
548822	2010 VG231	18.08	2.5645095	0.1785389	4.30907	104.44899	180.18738	Y
557505	2014 UB262	18.33	2.5644669	0.1812880	4.30940	105.44687	181.70689	Y
	2007 EH116	17.60	2.5632497	0.1837133	4.33016	104.12508	181.78781	Y
	2007 HC54	17.10	2.5630025	0.1852376	4.33060	103.90562	183.45131	Y
	2008 WV149	18.25	2.5616506	0.1860344	4.32935	105.32362	181.64195	Y
	2009 SY179	18.10	2.5638560	0.1808079	4.31363	105.25771	181.95983	
	2010 GN203	18.19	2.5616128	0.1827647	4.31768	105.51576	178.85422	Y
	2011 SU302	18.40	2.5613443	0.1843413	4.32594	105.00690	180.83267	Y
	2012 JM71	18.34	2.5643906	0.1803477	4.31944	104.45794	181.49202	Y
	2012 LN31	18.15	2.5645366	0.1805664	4.32084	104.18716	181.60272	Y
	2013 JG48	18.42	2.5640127	0.1804333	4.31002	105.27028	181.30120	
	2013 MW20	18.10	2.5640282	0.1789098	4.30379	105.82861	179.66519	Y
	2013 NA73	17.90	2.5645573	0.1778761	4.31150	104.20836	180.13663	Y
	2014 HH103	17.96	2.5628983	0.1818845	4.31303	105.17981	179.85773	Y
	2014 KY102	18.08	2.5643135	0.1802754	4.30634	105.52954	178.70247	
	2014 NN71	18.22	2.5656862	0.1796550	4.31314	104.34699	180.71664	
	2014 OG277	18.40	2.5655560	0.1824004	4.30982	105.58409	182.32744	
	2014 OJ66	18.94	2.5662203	0.1795922	4.30905	105.02988	179.79448	
	2014 PJ87	18.30	2.5657155	0.1814269	4.31509	105.41914	181.45122	
	2014 QL520	18.41	2.5655987	0.1802430	4.30661	105.04757	180.77744	
	2014 QQ580	18.83	2.5657832	0.1791684	4.31163	104.58123	180.17054	
	2015 FV225	17.60	2.5626639	0.1856256	4.32625	105.38305	182.32173	Y
	2015 HV138	18.70	2.5624216	0.1841988	4.32970	104.43650	181.05676	
	2015 KA91	17.90	2.5623849	0.1834933	4.32926	104.19929	180.34602	Y
	2015 KM237	19.48	2.5623846	0.1836411	4.33279	103.88926	180.72858	
	2015 OP104	18.00	2.5614614	0.1838197	4.32310	104.57302	180.62155	Y
	2015 PM156	18.40	2.5619337	0.1823281	4.32222	104.32621	179.28149	
	2015 PA184	19.20	2.5607541	0.1873221	4.32194	105.96144	182.84203	
	2015 XL282	17.79	2.5657472	0.1813020	4.31120	105.23265	181.11965	Y
	2016 GY256	18.24	2.5636554	0.1832090	4.32326	105.46202	182.61057	Y
	2016 GW276	18.48	2.5640705	0.1811033	4.31689	105.07693	181.94298	Y
	2016 GZ310	18.51	2.5642163	0.1812362	4.32011	104.87910	181.95655	Y
	2017 PA68	18.20	2.5644305	0.1794933	4.31098	104.94606	180.90470	
	2017 PK70	18.80	2.5631898	0.1834456	4.31379	105.99206	183.69467	
	2017 SM25	18.75	2.5641029	0.1805951	4.31554	104.93415	181.75945	
	2017 SQ83	18.33	2.5641221	0.1801750	4.31364	105.58058	180.54802	Y
	2017 WO47	18.12	2.5639686	0.1820342	4.32084	104.97053	181.94034	Y
	2018 NQ48	18.79	2.5649606	0.1809579	4.31287	105.27527	181.36440	
	2019 NP44	18.90	2.5614875	0.1835832	4.32402	104.94548	180.28464	Y
	2019 NB193	19.09	2.5616801	0.1826859	4.32590	104.31100	179.86577	
	2019 PS30	18.50	2.5613773	0.1841029	4.32102	105.34292	180.47624	Y
	2020 HQ57	18.50	2.5648348	0.1794839	4.31150	104.69543	180.06419	Y

Notes. Osculating heliocentric orbital elements at epoch MJD 60,200.0 from the MPC catalog: semimajor axis a, eccentricity e, inclination I, longitude of node Ω, and argument of perihelion ω. singleopposition orbits are listed at the end of the table. The third column gives the absolute magnitude H. The last column indicates, whether the asteroid has been detected by CSS during the phase 2 operations (Y=yes). We note a very small, singleopposition asteroids 2019 NF93, 2021 JQ73, 2023 JD27 and 2023 NV2 very likely members of the Hobson family too. However, their orbits, especially for 2019 NF93 based on observations spanning less than a week, are still very uncertain.

Table A.3. continued.

Asteroid	H (mag)	a (au)	e	I (deg)	Ω (deg)	ω (deg)	CSS
2020 KP36	19.11	2.5648730	0.1791752	4.31520	104.47316	179.58657	
2021 MO5	19.07	2.5636887	0.1815050	4.31175	105.50891	182.38281	
2023 JA22	18.24	2.5617572	0.1834690	4.32797	104.29884	180.14545	
– Singleopposition members –							
2014 JH120	18.70	2.5642333	0.1818812	4.31659	105.15400	180.80286	
2017 NY29	18.95	2.5644299	0.1787774	4.31392	104.20540	181.00297	
2019 GR115	18.80	2.5620456	0.1857152	4.32843	105.21081	181.52184	
2020 JM31	18.50	2.5636410	0.1836011	4.32256	105.32188	182.52160	
2020 OY50	18.60	2.5626675	0.1856940	4.32491	105.47980	182.45254	
2023 JZ8	18.67	2.5611412	0.1864161	4.32528	105.35980	181.88047	

Table A.4. Rampo family as of June 2023.

Asteroid		H (mag)	a (au)	e	I (deg)	Ω (deg)	ω (deg)	CSS
10321	Rampo	14.37	2.3285978	0.0952815	6.06091	53.88221	278.53547	Y
294272	2007 UM101	17.55	2.3294915	0.0944526	6.05304	53.16108	280.07932	Y
451686	2013 BR67	17.75	2.3278183	0.0943492	6.09428	61.69559	266.60300	Y
546329	2010 VO19	18.64	2.3284414	0.0929491	6.09152	62.49298	265.50211	Y
562123	2015 XH207	18.17	2.3273763	0.0941514	6.09700	62.36822	265.60187	Y
601678	2013 JF69	18.45	2.3287200	0.0936834	6.08492	60.24854	268.75113	Y
	2005 VO22	18.60	2.3284379	0.0942207	6.08237	60.44807	269.16712	Y
	2006 UA169	18.30	2.3287767	0.0936955	6.07318	58.37005	272.18424	Y
	2007 XP67	18.38	2.3290438	0.0937905	6.07805	58.76112	271.03067	Y
	2008 GZ170	18.33	2.3278729	0.0934523	6.08337	60.94947	268.37592	Y
	2008 SW341	18.33	2.3299539	0.0957301	6.04252	51.57990	282.43371	Y
	2009 HD95	18.15	2.3289378	0.0934420	6.08220	60.06838	269.21119	Y
	2009 SR371	18.70	2.3287466	0.0939626	6.06727	56.76277	274.96649	Y
	2009 WB276	18.46	2.3282859	0.0941812	6.06667	57.01124	274.26618	
	2010 VP264	18.71	2.3283338	0.0926865	6.10160	64.02540	263.22675	
	2011 WC22	18.63	2.3277415	0.0937305	6.09825	62.49161	265.21277	Y
	2012 VE126	18.70	2.3299965	0.0951578	6.05462	53.54667	279.68212	Y
	2013 RL101	18.10	2.3284038	0.0931685	6.08778	61.63153	267.08811	Y
	2013 VC30	18.53	2.3283365	0.0936238	6.07791	59.32627	270.66675	Y
	2013 VE51	18.78	2.3280528	0.0931012	6.09217	62.47444	265.73127	Y
	2014 HS9	18.38	2.3285282	0.0950748	6.07653	58.51435	271.58717	
	2014 HN87	19.03	2.3279516	0.0942568	6.09716	63.26309	264.63747	
	2014 ST44	18.97	2.3288418	0.0947150	6.06330	55.71611	275.58485	
	2015 BB184	18.71	2.3285590	0.0927376	6.09722	63.17079	264.60035	
	2015 HT91	18.22	2.3277235	0.0932915	6.08888	62.06807	266.70756	Y
	2015 TA367	18.89	2.3291271	0.0954163	6.05779	53.26353	279.52356	
	2015 TM372	18.57	2.3285477	0.0949021	6.07459	57.66486	273.16183	Y
	2015 VK190	19.02	2.3292421	0.0954998	6.04585	51.82977	282.18049	
	2016 GJ353	19.20	2.3296639	0.0942243	6.06093	54.67358	277.07351	
	2016 PR196	19.36	2.3298272	0.0945697	6.03487	50.33266	284.58940	Y
	2016 TE87	18.09	2.3281180	0.0941459	6.07157	57.95426	272.79711	Y
	2017 UH21	18.38	2.3289973	0.0933377	6.08745	60.32819	268.78683	Y
	2018 NN9	18.82	2.3281713	0.0946714	6.08543	59.97434	269.59068	
	2018 PS68	18.39	2.3291862	0.0955066	6.03521	49.93007	285.17948	Y
	2019 PC41	18.75	2.3285442	0.0939345	6.08000	59.64944	270.69700	Y
	2020 PJ53	18.90	2.3297760	0.0940307	6.05985	54.29035	278.19354	
	2021 QC81	19.05	2.3283427	0.0938521	6.08798	60.49374	268.42639	
	2022 QE61	18.93	2.3301748	0.0957688	6.03862	50.74900	283.82069	Y
	2022 QU76	19.08	2.3294832	0.0954286	6.05628	54.51791	278.35866	
	2022 QY123	18.97	2.3282912	0.0942403	6.09698	63.00157	264.91167	
			– Singleopposition members –					
	2020 MO19	18.70	2.3285350	0.0928385	6.09814	63.13642	264.21127	
	2022 RX76	18.99	2.3292702	0.0952251	6.06717	56.80863	274.65354	

Notes. Osculating heliocentric orbital elements at epoch MJD 60,000.0 from the MPC catalog: semimajor axis a, eccentricity e, inclination I, longitude of node Ω, and argument of perihelion ω. singleopposition orbits are listed at the end of the table. The third column gives the absolute magnitude H. The last column indicates, whether the asteroid has been detected by CSS during the phase 2 operations (Y=yes). We note two very small, singleopposition asteroids 2015 KM284 and 2015 KG287, very likely members of the Rampo family too. However, their orbits, based on observations spanning less than a week, are still very uncertain.

Table A.5. Wasserburg family as of June 2023.

Asteroid		H (mag)	a (au)	e	I (deg)	Ω (deg)	ω (deg)	CSS
4765	Wasserburg	14.05	1.9453591	0.0599697	23.71330	76.50142	108.59143	Y
350716	2001 XO105	18.00	1.9459411	0.0597860	23.70790	76.45874	108.33248	Y
	2012 KH56	19.22	1.9456701	0.0604509	23.70963	76.44694	108.32313	Y
	2016 GL253	19.18	1.9457396	0.0598318	23.71026	76.46677	108.53996	Y
	2017 DU131	18.90	1.9456063	0.0604246	23.70749	76.42791	108.29692	Y
	2017 KO46	19.27	1.9453538	0.0604115	23.70825	76.50900	108.09233	Y
	2018 YF16	18.94	1.9454573	0.0602688	23.70620	76.40472	108.19370	Y
	2020 HF21	19.01	1.9455092	0.0604480	23.70669	76.45580	108.27241	Y

Notes. Osculating heliocentric orbital elements at epoch MJD 60,000.0 from the MPC catalog: semimajor axis a, eccentricity e, inclination I, longitude of node Ω, and argument of perihelion ω. The third column gives the absolute magnitude H. The last column indicates, whether the asteroid has been detected by CSS during the phase 2 operations (Y=yes).

Table A.6. Martes family as of June 2023.

Asteroid		H (mag)	a (au)	e	I (deg)	Ω (deg)	ω (deg)	CSS
5026	Martes	14.10	2.3785050	0.2419535	4.28293	304.74872	17.59761	Y
	2005 WW113	17.92	2.3766591	0.2431729	4.29300	304.86627	17.41694	Y
	2010 TB155	17.90	2.3771299	0.2421036	4.28760	304.75606	17.10483	Y
	2011 RF40	19.87	2.3771146	0.2442609	4.29445	304.60737	17.41062	
	2022 QB59	20.10	2.3770235	0.2441532	4.29430	304.61079	17.40973	
	2022 RM50	20.13	2.3769466	0.2440863	4.29433	304.61266	17.38851	

Notes. Osculating heliocentric orbital elements at epoch MJD 60,000.0 from the MPC catalog: semimajor axis a, eccentricity e, inclination I, longitude of node Ω, and argument of perihelion ω. The third column gives the absolute magnitude H. The last column indicates, whether the asteroid has been detected by CSS during the phase 2 operations (Y=yes).

Table A.7. Lucascavin family as of June 2023.

Asteroid		H (mag)	a (au)	e	I (deg)	Ω (deg)	ω (deg)	CSS
21509	Lucascavin	15.06	2.2804908	0.1126543	5.98061	70.14627	4.71189	Y
180255	2003 VM9	17.21	2.2806359	0.1126433	5.98101	70.37821	4.12878	Y
209570	2004 XL40	17.24	2.2815589	0.1114265	5.97968	69.95755	4.92455	Y

Notes. Osculating heliocentric orbital elements at epoch MJD 60,000.0 from the MPC catalog: semimajor axis a, eccentricity e, inclination I, longitude of node Ω, and argument of perihelion ω. The third column gives the absolute magnitude H. The last column indicates, whether the asteroid has been detected by CSS during the phase 2 operations (Y=yes).